

Improving Forecasts of Persistent Contrails through Ice Deposition Adjustments

Zane Dedekind¹, Alexei Korolev¹, and Jason A. Milbrandt¹

¹Meteorological Research Division, Environment and Climate Change Canada, Toronto, Ontario, Canada

Correspondence: Zane Dedekind (zane.dedekind@ec.gc.ca)

Abstract. Aviation-induced clouds, especially persistent contrails, contribute significantly to anthropogenic climate forcing, often surpassing the short-term impact of aviation CO₂ emissions. These clouds form in ice-supersaturated regions, where they trap longwave radiation and warm the climate. On 25 November 2023, widespread ice-supersaturated layers over eastern Canada and the USA led to extensive contrail formation, confirmed by GOES-16 satellite imagery and ground-based photography. Atmospheric conditions were characterized using ceilometer data from Toronto Pearson Airport and radiosonde soundings.

High-resolution simulations were ~~conducted~~ performed using the Global Environmental Multiscale (~~GEM~~) ~~model~~ model coupled with the Predicted Particle Properties (P3) microphysics scheme. ~~The Contrail Avoidance Tool (CoAT), incorporating Schmidt-Appleman Criteria and a wake-vortex model, simulated persistent contrail formation and properties. Sensitivity tests adjusting ice-depositional growth rates evaluated their impact on ice supersaturation. Results indicate that the control (CNTL) simulation underestimated relative humidity over ice (-), a common limitation where moisture is depleted too rapidly. Reduced depositional growth rates improved forecasts and contrail-forming regions. However, GEM-CoAT underestimated contrail depth and ice number concentration in very shallow high-layers. CoAT simulations also revealed that SAC alone is insufficient, as wake-vortex dynamics can induce adiabatic warming, leading to ice particle sublimation. A deposition-adjusted simulation incorporating the deposition coefficient reduced ice particle growth rates and enhanced upper-tropospheric moisture buildup, shifting the relative humidity with respect to ice peak from ~102% to ~108%, closer to observations.~~

~~Further analysis examined contrail formation for two aircraft types (The Contrail Avoidance Tool, a diagnostic for identifying and forming persistent contrails, was then applied to simulate persistent contrails for an A321 and a B747) under varying soot emission regimes. The B747 generated deeper wake vortices, enhancing adiabatic heating and reducing maintained higher contrail ice number concentrations by 27% in sensitivity simulations and 78% in the CNTL simulations. Adjusting depositional growth rates allowed GEM-CoAT to accurately simulate contrail formation and persistence (CINC) because its higher fuel flow injected more soot per flight distance, partly offset by wake-vortex sublimation. Consequently, a low-soot B747 produced CINC comparable to an A321 burning conventional Jet A fuel. Aircraft-specific wake dynamics and soot regimes jointly control ice crystal survival, indicating that contrail models using constant soot emission indices without accounting for wake-vortex losses may overestimate contrail ice production and possibly contrail radiative impacts.~~

1 Introduction

Contrails, or condensation trails, are linear ice clouds that form in the wake of aircraft flying at high altitudes where the ambient atmosphere is sufficiently cold, typically colder than -40°C , and humid. These artificial clouds originate from the mixing of hot, moist exhaust gases with the surrounding air, leading to rapid condensation ~~and freezing~~ of water vapor onto emitted particles, such as soot and other aerosols (Schumann, 1996; Kärcher, 2018) followed by near-instantaneous freezing. While some contrails dissipate quickly, ~~others persist and spread into contrail cirrus if persistent contrails form when~~ the environmental air is ice-supersaturated ~~, which can contribute to~~ (i.e. relative humidity with respect to water, $\text{RH}_i \geq 100\%$), allowing ice crystals to grow rather than sublimate. Such persistent contrails may either retain their linear shape or spread into contrail cirrus, thereby contributing to cloud cover and significantly ~~alter the radiative balance of the Earth's atmosphere~~ altering the Earth's radiative balance (Kärcher, 2018; Lee et al., 2023).

The aviation industry is a significant contributor to anthropogenic climate change, accounting for approximately 3.5 % of total effective radiative forcing (ERF) as of 2018 (Kärcher, 2018; Lee et al., 2021). Notably, about two-thirds (66 %) of this warming impact is attributed to non- CO_2 effects, primarily from contrail cirrus and nitrogen oxide (NO_x) emissions. The radiative forcing from contrail cirrus alone is estimated to be 57.4 mW m^{-2} , making it the single largest contributor to aviation-induced climate effects, surpassing the impact of cumulative CO_2 emissions from aviation, which is 34.3 mW m^{-2} (Lee et al., 2021).

Contrail cirrus exerts a complex influence on Earth's energy balance. While they reflect some incoming solar radiation, their primary effect is trapping outgoing longwave radiation, leading to a net warming impact. The strength of this effect depends on atmospheric conditions, contrail properties, and flight patterns. Studies indicate that contrail-induced cloudiness covers up to 10 % of the sky area in high-traffic regions such as Europe and North America (Burkhardt and Kärcher, 2011).

Given the projected growth in global aviation, which is expected to double its CO_2 emissions by 2050 without mitigation strategies (Lee et al., 2009), understanding and addressing contrail-induced climate effects is a critical research priority. Several mitigation strategies have been explored, including optimizing flight altitudes and routes, reducing soot emissions by transitioning to low-aromatic or biofuel blends, using hydrogen fuels, and employing alternative aircraft propulsion technologies (Burkhardt et al., 2018; Teoh et al., 2020, 2022; Lottermoser and Unterstraßer, 2025). Studies suggest that targeted rerouting of just 2 % of flights could reduce contrail radiative forcing by up to 59 % with negligible fuel penalties over Japanese airspace while rerouting 12 % of flight reduce the radiative forcing by 80 % over the North Atlantic (Teoh et al., 2020, 2022).

Simulating Accurately simulating the evolution of contrail ice number concentration (CINC) is crucial for ~~accurately~~ predicting contrail persistence and lifetime. Ice crystal number concentration directly influences contrail optical depth, growth rates, and sedimentation, which in turn determine their overall climate impact. Higher CINC lead to greater optical thickness and longer persistence, whereas lower CINC promote faster ice particle sedimentation and sublimation, reducing contrail lifes-

pan. The initial CINC is strongly controlled by soot emissions from different fuel types, where soot-rich ($> 10^{15}$ (kg-fuel) $^{-1}$) exhaust from conventional Jet A-1 fuels produces abundant ice-forming particles and high CINC. In contrast, in soot-poor exhaust, ultrafine aqueous plume particles can form if condensable vapours are present, contributing to ice formation at very low ambient temperatures, while low-soot alternative fuels (10^{13} (kg-fuel) $^{-1}$ – 10^{14} (kg-fuel) $^{-1}$) generally yield fewer ice crystals and shorter-lived contrails if ultrafine particle formation cannot be avoided (Kärcher and Yu, 2009; Kärcher, 2018)

Several parameterizations have been developed to better represent contrail microphysics and ice crystal evolution. Schumann (2012) introduced the Contrail Cirrus Prediction Tool (CoCiP), a fast process-based model designed to estimate contrail properties based on meteorological conditions and aircraft emissions. Lewellen and Lewellen (2001); Lewellen (2014) applied large-eddy simulations to investigate wake vortex dynamics and their impact on contrail ice crystal formation, showing how turbulence influences contrail spreading and persistence. ~~Unterstrasser (2016) developed a parameterization that enhances the representation of contrail-to-cirrus transitions, improving the understanding of how environmental conditions, including ice supersaturation, affect contrail growth and dissipation.~~ Nevertheless, turbulence is generally of secondary importance, with shear and sedimentation identified as the dominant processes controlling contrail spreading (Lewellen, 2014; Unterstrasser and Gierens, 2014). Lewellen et al. (2014) and Lewellen (2014) employed large-eddy simulations with size-resolved microphysics to follow contrails from their formation a few wing spans behind the aircraft through many hours of evolution, highlighting the roles of turbulence, crystal loss, and radiative feedbacks. Unterstrasser (2016) complemented this by developing a parameterization for the formation and properties of young contrails, while Unterstrasser et al. (2017a, b) extended the analysis to contrail–cirrus interactions with natural cirrus. Together, these studies using large-eddy simulations capture the progression from contrail initiation to their full development into cirrus-scale, including the conditions under which contrails lose their distinct identity once embedded in surrounding cirrus.

80 The persistence and variability of ice supersaturation in ice clouds are strongly influenced by the deposition coefficient (α_D), which describes the efficiency of water vapor molecules attaching to ice crystal surfaces. Laboratory studies, including wind tunnel experiments, cloud chambers, and cold-stage scanning electron microscopy imaging, have shown that α_D is not constant but varies with temperature, supersaturation, and ice crystal habit. Measurements by Fukuta and Takahashi (1999), Lamb et al. (2023), and Harrington and Pokrifka (2024) reveal that α_D often falls well below unity under cold, upper-tropospheric conditions typical of cirrus, indicating kinetic limitations to depositional growth. These studies also identify supersaturation thresholds associated with morphological transitions of ice crystal shapes, such as hollowing, providing physical constraints on when and how efficiently ice crystals grow.

From a modeling perspective, simplified treatments that assume $\alpha_D = 1$ or ~~apply~~ applying a saturation adjustment fail to capture the observed frequency and magnitude of ice-supersaturated regions. Gierens et al. (2003, 2020) and (Sperber and Gierens, 2023) showed that such assumptions result in systematic underprediction of supersaturation and contrail persistence in numerical weather and climate models. To address this, Kärcher et al. (2023) incorporated supersaturation-dependent deposition coefficients, based on laboratory constraints from Lamb et al. (2023), into stochastic parcel models coupled with gravity wave-induced temperature fluctuations. Their simulations reproduced both the mean and variability of in situ supersaturation

measurements, highlighting the role of depositional kinetics in ice cloud microphysics. Together, laboratory and modeling work shows the need for physically-based representations of α_D to accurately simulate ice cloud evolution.

This study investigates how variations in the depositional growth of ice, calculated by adjusting α_D , affect the extent and persistence of ice-supersaturated regions and the properties of contrails within a high-resolution numerical weather prediction (NWP) framework. We explore the following questions:

- How does the adjustment of the ice deposition rate, through changes in the deposition coefficient, influence the persistence and intensity of ice-supersaturated regions?
- In what ways does the deposition rate impact contrail formation processes and the resulting CINC within young contrails?
- To what extent do wake vortex dynamics, particularly adiabatic heating during plume descent, limit contrail formation despite favorable Schmidt–Appleman ~~Criteria-criterion~~ (SAC) ~~conditions?~~ and ice-supersaturated conditions?
- How do soot emission regimes across different fuel types control CINC and thereby influence contrail formation and persistence?

The remainder of this paper is organized as follows: Section 2 describes the methods, including an overview of the synoptic environment, observational datasets, and the modeling tools used to simulate contrail formation. Section ~~3 presents the results of sensitivity experiments examining how variations in the depositional growth rate affect the , contrail ice number concentrations, and contrail persistence~~ 3.1 focuses on the role of the deposition coefficient. Sections 3.1.1 and 3.1.2 compare the deposition-adjusted control (CNTL-DA) simulation to the control (CNTL, where $\alpha_D = 1$) simulation and examine the resulting impacts on upper-tropospheric RH_i. Section 3.1.3 contrasts the two simulations over the Toronto region and discusses their implications for persistent contrail-forming conditions. Section 3.2 investigates the sensitivity of contrail formation and persistence to varying soot emission regimes within the deposition-adjusted (DA) simulations. Section 4 discusses the broader implications of these findings. ~~The paper concludes with,~~ followed by a summary of key ~~findings results~~ and recommendations for improving contrail representation in weather and climate models. Appendix A provides the physical basis and equations ~~governing describing~~ the depositional growth of ice crystals and ~~how the deposition coefficient α_D influences ice particle mass growth under supersaturated~~ the influence of the deposition coefficient α_D under ice-supersaturated conditions.

2 Methods

2.1 Synoptic conditions and observational data

On ~~25Nov-~~ Nov 2023, a large ice-supersaturated region formed, leading to extensive cirrus cloud formation over the southeastern and northeastern parts of Canada and the USA, respectively. The upper-level atmospheric conditions included a deep trough in the jet stream which allowed cold Arctic air to plunge southward into the Great Lakes region. This created significant

temperature contrasts and instability in the upper troposphere. Evidence from radiosonde soundings, satellite observations, and surface-based photography confirmed the presence of ice-supersaturated layers aloft, within which cirrus clouds and persistent contrails formed (Fig. 1b-d).

2.1.1 Radiosonde data

Upper-air radiosonde data were obtained from the University of Wyoming dataset (University of Wyoming, 2024). The radiosonde data encompassed the balloon's precise trajectory, detailing latitude, longitude, altitude, and time. This information is crucial, as radiosondes can drift significantly from their launch sites during ascent. Balloons may drift approximately 5 km in the mid-troposphere, around 20 km in the upper troposphere (Seidel et al., 2011). ~~Radiosonde data was collected to determine the drift distance~~ Knowing the balloon's trajectory enables matching its observations to the nearest model grid point in both space and time. For example, a balloon launched at 12 UTC requires several minutes to reach cruising altitude, so temporal alignment is also necessary. The drift distance was therefore calculated between the launch ~~location site~~ and the 300 hPa pressure level (approximately jet cruising altitude) for ~~various stations at 1200~~ multiple stations at 12 UTC on ~~25 November~~ Nov 2023 (Table 1).

Table 1. Radiosonde Drift Distances at 300 hPa at 1200 UTC on 25 Nov 2023

Station Name	Location	Station Identifier	Drift Distance (km)
Albany	NY, USA	ALB	31.23
Gaylord	MI, USA	APX	25.22
Buffalo	NY, USA	BUF	23.23
White Lake	MI, USA	DTX	19.96
Green Bay	WI, USA	GRB	23.44
International Falls	MN, USA	INL	34.12
Maniwaki	QC, Canada	WMW	42.42
Pickle Lake	ON, Canada	WPL	41.82

Assuming a balloon ascent rate of 5 m s^{-1} , the time to reach the 300 hPa pressure level is approximately ~~30.5~~ 30 min if the balloon drift is ignored. However, considering potential variations in ascent rates and balloon drift, the actual time can range between 40 min and 110 min. For modeling purposes, we assume an ascent time of approximately 50 min to align the model data with the balloon's arrival at the 300 hPa level.

2.1.2 Satellite data

The Advanced Baseline Imager (ABI) aboard the GOES-R series satellites is a passive imaging radiometer featuring 16 spectral bands, including 10 in the infrared spectrum. The spatial resolution for these infrared bands is 2 km (Kalluri et al., 2018). In its operational modes, the ABI provides full-disk imagery every 10 min, images of the contiguous ~~United States (CONUS)~~ US

(every 5 min, and two mesoscale images every 60 s (or one every 30 s). Among its capabilities, the ABI utilizes a "Dust" RGB (Red-Green-Blue) composite to detect and monitor airborne dust. This product is also especially useful to detect contrails. This composite combines data from infrared channels 8.4 μm (Band 11), 10.3 μm (Band 13) and 12.3 μm (Band 15). The GOES-16 data was downloaded from University of Utah (2020) and the "Dust" RBG was generated using the software package from
 150 Blaylock (2023).

2.1.3 Aircraft flight data

- **Data Source:** Flight data was obtained from Flightradar24 (Flightradar24, 2024).
- **Selected Flights:** A subset of flights was identified as potential contributors to contrail formation (Fig. 1a and Table 2). These flights cruised at altitudes ranging from 8,800 m to 10,700 m (29,000 ft to 35,000 ft).
- 155 – **Recorded Data Points:** Flight data was recorded at ~~30 s~~ 30-s intervals, during which aircraft traveled approximately 6 to 7 km at cruising speed between recordings. The data was then interpolated onto a 1 km \times 1 km grid, aligning with the model grid resolutionspacing, ensuring one recording per grid point.

Table 2. Aircraft Wingspan and Cruising Altitude Data

Aircraft Identifier	Aircraft Type	Wingspan (m)	Cruising Altitude (ft)	~Time of Toronto Flyover (UTC)
TK6061	B747	64.4	31,000	1345
CV6686	B747	64.4	34,000	1315
AS459	B747	64.4	34,000	1330
DL384	A321	35.8	30,000–34,000	1245
AA2455	A321	35.8	34,000	1330
UA364	A319	35.8	34,000	1415
UA311	B757	38.0	34,000	1345

2.1.4 Ceilometer at CYYZ

The Ceilometer, CHM 15k Cloud Height Meter, is an advanced light detection and ranging (LIDAR-based) remote sensing
 160 instrument deployed at Toronto Pearson International Airport (CYYZ) to measure cloud height, penetration depth, and vertical visibility. Operating at a ~~15 s~~ 15-s temporal resolution, it employs the lidar techniqueNe-YAG laser ($\lambda = 1064 \text{ nm}$) to emit short laser pulses into the atmosphere. These pulses scatter upon interaction with aerosols and cloud particles, with the backscattered signal being analyzed to determine cloud structure and visibility conditions.

The CHM 15k is capable of measuring up to 15 km in altitude with a range resolution of 5–15 m, depending on the mea-
 165 surement mode. Its full waveform analysis allows for the identification of multiple cloud layers (up to 9), 3 layers in its current

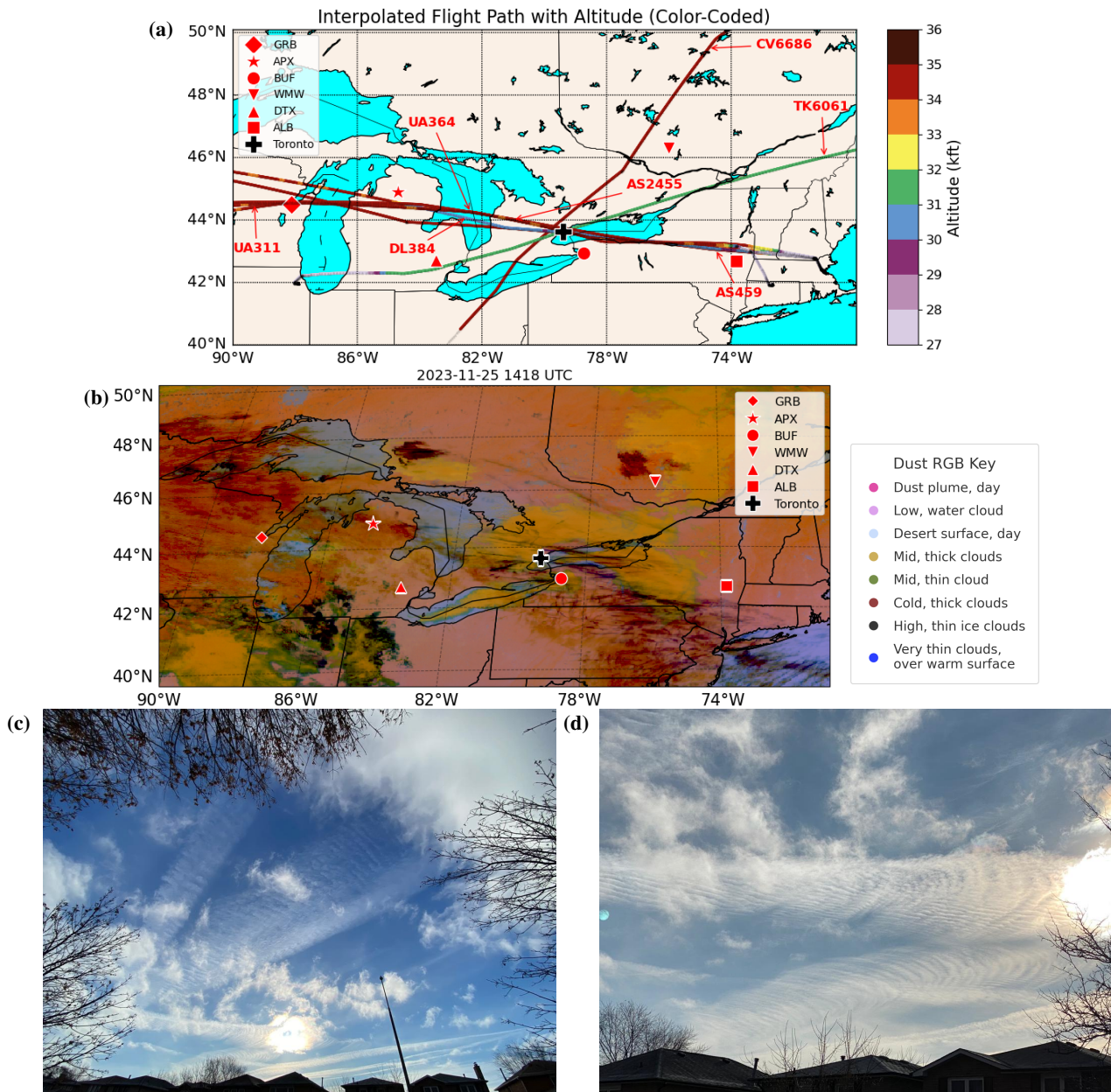


Figure 1. (a) Interpolated flight paths and sounding stations (b) GOES-16 Dust RGB and sounding stations at 1430 UTC (c) and (d) photos taken from Toronto, Canada at 1420 UTC by Alexei Korolev. [The names of the abbreviated sounding stations \(red markers\) can be found in Table 1.](#)

configuration, and provides high-resolution backscatter profiles. It ~~utilizes~~ uses photon counting technology, enhancing detection sensitivity and minimizing background noise. The system records parameters such as cloud base height, penetration

depth, maximum detectable range, vertical visual range, and sky condition, making it crucial for aviation meteorology and atmospheric research.

170 2.2 Model

2.2.1 Atmospheric model and initialization

The Global Environmental Multiscale (GEM) model is a versatile atmospheric modeling system widely used for high-resolution simulations of atmospheric processes (Côté et al., 1998; Girard et al., 2014). ~~The integration of the Predicted Particle Properties (P3) microphysics scheme into GEM represents a significant advancement in the modeling of ice-phase hydrometeors and mixed-phase cloud dynamics. This methodology outlines the configuration and application of the GEM-P3 setup as described in several studies (Morrison and Milbrandt, 2015; Milbrandt and Morrison, 2016; Milbrandt et al., 2021; Qu et al., 2022; Cholette et al., 202~~

~~GEM serves as the operational NWP model for all atmospheric prediction systems at Environment and Climate Change Canada. GEM has a non-hydrostatic, fully compressible dynamical core using semi-Lagrangian advection and a terrain-following hybrid vertical coordinate system (Côté et al., 1998; Girard et al., 2014). This configuration is suitable for a wide range of resolutions, from mesoscale to cloud-resolving scales. Our simulations For this study, we use a horizontal grid spacings of $1\text{ km} \times 1\text{ km}$ over a 1600×1000 limited-area domain centered at 45.2°N and $-79.979.9^\circ\text{E-W}$ (eastern Canada). Typically, 60 vertical levels are used in operational systems using GEM, but here, Fig. 1a). Our simulations use lateral and surface boundary conditions from the operational 2.5-km High Resolution Deterministic Prediction System (HRDPS; Milbrandt et al., 2016), updated hourly. We use 121 vertical levels are used to enhance the vertical resolution in the upper tropical troposphere with grid spacings of $\sim 230\text{ m}$ at 300 hPa to capture hPa for a more accurate representation of ice supersaturated regions better. GEM uses lateral and surface boundary conditions obtained from the operational 2.5-km High Resolution Deterministic Prediction System (HRDPS; Milbrandt et al., 2016), which is updated hourly. A 30 s model timestep is. A 30-s model timestep was used, with the model initialized at 0600 UTC and running for a duration of 13 h.~~

190

2.2.2 Cloud microphysics scheme

~~The The integration of the Predicted Particle Properties (P3 microphysics scheme is unique in that the ice phase uses the) bulk microphysics scheme into GEM represents a significant advancement in the modeling of ice-phase hydrometeors and mixed-phase cloud dynamics. This methodology outlines the configuration and application of the GEM-P3 setup as described in several studies (Qu et al., 2022; Cholette et al., 2024; Korolev et al., 2024).~~

195

2.2.2 Cloud microphysics scheme

The P3 microphysics scheme uses a property-based approach treatment of the ice phase (i.e. Jensen et al., 2017), in contrast with the traditional approach of predefined ice-phase categories (i.e. ice, snow, graupel and hail), whereby all ice-phase or mixed-phase particles are represented by one or more generic or "free" categories whose bulk physical properties, such as mass, number, density, and rime fraction, evolve freely and continuously. This enables each ice category to represent a wide range of dominant types of ice and removes the need for artificial "conversion" between categories. With the use of multiple free ice-phase categories, multiple modes—i.e., i.e., populations of ice with different bulk properties—, can exist in the same point in time and space. A complete description of the original P3 scheme can be found in Morrison and Milbrandt (2015) and Milbrandt et al. (2016); descriptions of subsequent major developments can be found in Milbrandt et al. (2021), Cholette et al. (2024), and Morrison et al. (2025). In this study, the two-moment ice configuration, with prognostic liquid fraction off, and with 3 ice categories is used.

Hydrometeor size distributions, including those of the liquid categories ("cloud" and "rain"), are represented by complete 3-parameter gamma functions, with shape and slope parameters evolving dynamically based on the prognostic variables. The configuration uses the two-moment treatment of ice particles instead of the triple-moment treatment which is more relevant approach (Milbrandt et al., 2021; Morrison et al., 2025), the latter being more important for deep convective systems to better resolve size sorting and improve simulations better and improve the simulation of hail and heavily rimed particles. Additionally, at the time of preparing this study, the "full" 3-moment version of P3 Morrison et al. (2025) was not yet available. In this version, the With triple-moment ice the spectral dispersion changes due to deposition/sublimation which; this could be a topic of future work for contrails.

To examine the impact of the deposition coefficient (α_D , from equation A2) on the vapor depositional mass growth of ice crystals (equation A1) and its subsequent effect on contrail persistence, we conducted sensitivity simulations. These simulations introduce reduction factors (rf) to adjust the depositional growth of ice particles heuristically.

depositional mass growth ratio (dgr) which was implemented into P3.

$$\frac{\left(\frac{dm}{dt}\right)_{\alpha_D}}{\left(\frac{dm}{dt}\right)_{\alpha_D=1}} \left(\frac{dm}{dt}\right)_{\alpha_D} = rf, \quad \text{where } rf \in \{0.6, 0.8, 0.9\} \left(\frac{dm}{dt}\right)_{\alpha_D=1} \times dgr \quad (1)$$

The reduction factor rf is determined by varying the dgr is computed offline as the ratio of depositional growth rates for $\alpha_D = 1$ and for α_D varying with T , P , humidity, and ice particle size and computing the corresponding α_D . These size-dependent. This dgr , being dependent on ambient conditions and ice particle size, serves as a multiplicative factor in the P3 scheme (Eq. 1). The deposition adjustment was implemented only in the upper troposphere for $T < -38^\circ\text{C}$ consistent with laboratory and modeling studies (Fukuta and Takahashi, 1999; Gierens et al., 2003; Lohmann et al., 2008; Skrotzki et al., 2013; Lamb et al., 2013). The use of α_D values are then used to calculate the depositional growth rate, which is subsequently compared to the reference case where $\alpha_D = 1$ in the depositional growth rate equation used here in P3 is not included in the CoAT framework; hence, ice crystal formation and loss during the vortex phase are independent of α_D . Further information on this approach can be found in Appendix A.

2.2.3 Contrail model: Contrail Avoidance Tool (CoAT)

The formation of contrails, governed by the ~~Schmidt–Appleman Criterion (SAC)~~SAC, requires specific thermodynamic conditions that depend on both atmospheric and aircraft parameters. A critical parameter in this framework is the slope of the mixing line, G , which characterizes the relationship between the parameters of the exhaust plume and the ambient atmosphere.

235 According to ~~Schumann (2012)~~Schumann (1996), G is expressed as:

$$G = \frac{c_p \cdot p \cdot EI_{H_2O}}{\left(\frac{M_{H_2O}}{M_{air}}\right) \cdot Q \cdot (1 - \eta)}, \frac{c_p p EI_{H_2O}}{(M_{H_2O}/M_{air}) Q (1 - \eta)} \quad (2)$$

where c_p is the specific heat capacity of air at constant pressure ($1004 \text{ J kg}^{-1} \text{ K}^{-1}$), p is the ambient pressure (Pa), EI_{H_2O} is the water emission index (~~kg of H_2O / 1.25 kg of H_2O~~ per kg of fuel burned), M_{H_2O}/M_{air} is the molar mass ratio of water to air (approximately 0.622), Q is the specific combustion heat of the fuel (43.2 MJ kg^{-1} for kerosene), and η is the propulsion efficiency (0.29).

For contrails to form, the ambient temperature T must be below the maximum threshold temperature, defined as the temperature at which the mixing line intersects the liquid water saturation curve (Schumann, 2012). ~~Additionally, This ensures that~~ the relative humidity over water ~~must exceed~~exceeds the critical threshold ~~to ensure that the water vapor in the exhaust can condense~~required for condensation of exhaust water vapor. Under these conditions, water vapor condenses and freezes ~~on~~ aerosols onto soot and ambient aerosol particles, forming ice particles. These ice particles grow by water vapor deposition, and if crystals that subsequently grow by vapor deposition. If ice supersaturation persists, ~~the contrails can~~ (i.e., $RH_i \geq 100\%$), contrails can remain and evolve into long-lived clouds: cirrus. Although Li et al. (2023) demonstrated that contrails may persist under ice-subsaturated conditions, for consistency with the parameterization of Unterstrasser (2016), which assumes formation and growth under ice-supersaturated conditions—we restrict persistence to regions where ice supersaturation is maintained.

250 The wake vortex phase of contrail evolution involves distinct processes in the primary and secondary wakes, critical for understanding contrail dynamics and their transition into cirrus clouds. The primary wake, associated with the counter-rotating vortex pair generated by the aircraft's lift, experiences strong downward motion, leading to adiabatic heating and partial sublimation of ice particles. These dynamics, which trap a significant portion of the exhaust within the vortex pair, are strongly influenced by environmental factors such as temperature and relative humidity (Sussmann and Gierens, 1999; Unterstrasser, 255 2016). In contrast, the secondary wake forms a "curtain" of detrained exhaust between the original emission altitude and the descending vortex. Ice particles in the secondary wake grow through deposition in an ice-supersaturated environment and retain the majority of the contrail ice mass by the end of the vortex phase. This secondary wake, less affected by adiabatic heating, plays a crucial role in the persistence and spreading of contrails (Unterstrasser, 2014; Lewellen, 2014; Unterstrasser, 2016).

When the conditions for ~~T and SAC~~and for contrail persistence (RH_i ~~from the SAC~~ $\geq 100\%$) are satisfied, GEM uses the wake vortex model from Unterstrasser (2016), which focuses on the interaction between ice microphysics and wake vortex dynamics. The Unterstrasser (2016) parameterization provides a framework for quantifying key characteristics of young contrails during their early development phases. It calculates the maximum vertical displacement of wake vortices and the vertical extent

of the contrail, which corresponds to the maximum vortex displacement if ice particles can survive the warming effects associated with the adiabatic descent of the vortices. Additionally, it estimates the survival fraction of contrail ice particles, accounting for their loss due to changes in relative humidity resulting from adiabatic warming and incorporating the influence of ice supersaturation, ~~temperature~~ T , and the Kelvin effect on crystal growth (~~Jensen et al., 2024~~) (~~Lewellen, 2012; Jensen et al., 2024~~). The wake vortex model uses the aircraft information from Table 2 and the atmospheric conditions (e.g. ~~temperature, pressure, humidity~~ i.e. T , P , RH_i and the static stability of air) from GEM to determine ice particle survival, the ~~contrail ice number concentration~~ CINC and the vertical contrail extent of young contrails during the first 5 min. The wake vortex model enables parameterizations to incorporate additional aircraft characteristics, such as weight, speed, and fuel flow rate. However, for our purposes, we utilized only the parameterization based on wingspan ~~for further calculations. To estimate the contrail ice mass concentration~~. Given the aircraft wingspan b_{ws} and the ice crystal emission index EI_{iceno} (equal to the soot emission index), the water vapor emission rate I_0 is estimated by

$$I_0 = 0.02 \text{ kg m}^{-1} \left(\frac{b_{ws}}{80 \text{ m}} \right)^2 \quad (3)$$

from which the initial number of emitted ice crystals N_0 can be derived as

$$N_0 = \frac{I_0}{EI_{H_2O}} EI_{iceno} \cdot \quad (4)$$

After the vortex phase the contrail ice crystals which survived the vortex phase (CI_{surv}), is defined by

$$CI_{surv} = N_0 \times f_{Ns} \cdot \quad (5)$$

where f_{Ns} is the fraction of ice crystals surviving the vortex phase. The I_0 and CI_{surv} per flight meter are distributed over the flight segment within each GEM grid cell and converted to the volumetric prognostic variables during one time step as

$$CINC = \frac{CI_{surv} f_d}{V_g}, \text{ and} \quad (6)$$

$$CQI = \frac{I_0 f_d}{V_g}, \quad (7)$$

where CINC (m^{-3}) and the ~~sublimated ice particles from the primary vortex are converted into water vapor and incorporated into the plume's water vapor budget. The surviving ice particles grow through deposition, assuming spherical geometry for the ice particles (Pruppacher and Klett, 2010). The resulting contrail~~ contrail ice mass concentration (CQI, kg m^{-3}) is of young contrails, f_d is the flight distance within a grid box and V_g is the volume of the grid box. When assessing contrail persistence for individual flights (Table 2), not contrail-forming regions and their associated properties, the CINC and CQI contributions after the vortex phase are added to the cloud ice number and mass concentrations ~~derived from the wake vortex model are from the microphysics scheme. These combined quantities are referred to as the total ice number concentration and total ice mass~~

concentration, which are subsequently advected by GEM-'s advection scheme. If the contrail's vertical extent exceeds that of the model grid, the contrail's ice content is distributed uniformly into the model grid box below the flight level (Appendix A2). This adjustment is necessary because the Unterstrasser (2016) scheme was developed for a single, constant-RH_i layer. In contrast, our model resolves contrail properties within discrete grid cells that may be shallower than the diagnosed contrail depth. When the simulated contrail depth exceeds a grid layer, the CINC can be confined within that grid box—leading to an overestimation of the CINC and an underestimation of the wind-shear effects—or redistribute it downward into the grid box below, where RH_i may be lower than the value used to diagnose CINC. Both choices have limitations, but we also adopt the latter approach to include impacts from vertical wind shear, promoting vertical spreading.

300 3 Results

~~Here, we present two distinct simulation approaches, along with the sensitivity simulations, for analyzing contrail formation. First, we conducted simulations assuming the characteristics of an A321 aircraft and a B747 aircraft uniformly across the entire domain. This approach allowed us to generate metrics such as contrail depth, contrail ice number concentration (CINC),~~ Unterstrasser (2016) found that, on average, CI_{surv} shows the strongest sensitivity to EI_{iceno} and RH_i. Soot number emission indices, represented here by EI_{iceno}, are often explored over several orders of magnitude to represent engine or fuel regimes. In contrail formation studies, soot emission indices (EI_{soot}) delineate microphysical regimes controlling the origin and number of ice crystals. The Very-High-Soot (VHS) and High-Soot (HS) regimes (EI_{soot} ≥ 10¹⁵ kg⁻¹) represent the soot-rich regime described by Kärcher and Yu (2009); Kärcher et al. (2015), where nearly all emitted soot particles act as freezing nuclei and ice forms predominantly by homogeneous freezing around soot cores. The Normal-Soot (NS) regime (EI_{soot} ~ 10¹⁴ kg⁻¹) corresponds to the intermediate regime, in which ice formation transitions from soot-driven to mixed liquid-soot contributions, leading to a tenfold reduction in ice number concentration compared to the soot-rich case. Finally, the Low-Soot (LS) regime (EI_{soot} < 10¹³ kg⁻¹) aligns with the soot-poor regime, where contrail ice forms primarily on entrained atmospheric particles or ultrafine plume particles rather than soot, yielding fewer but larger ice crystals and substantially lower contrail optical depth (Kärcher and Yu, 2009; Kärcher et al., 2015).

315 2.0.1 Tracking flight-induced contrails from GEM output

To quantify contrail persistence and its influence on cirrus cloud properties, we identify and track the regions associated with the persistent contrails over Toronto on 25 Nov 2023 (Fig. 1). This region spans 310 hPa to 290 hPa, where RH_i ≥ 100%, and corresponds to the layer in which two flights (DL384 and TK6061) generated contrails. The DA-VHS simulation, which produce the longest-lived contrail, is used to define this region. We calculate the 99.5th percentile of the total ice column density (TICD) from the DA-VHS simulation (described in the next section), which provides the strongest and most coherent

contrail signal, and use it to construct a binary mask $M(x, y, t)$ defined as

$$M(x, y, t) = \begin{cases} 1, & \text{if } \text{TICD}_{\text{VHS}}(x, y, t) \geq P_{99.5}^{\text{VHS}}, \\ 0, & \text{otherwise.} \end{cases} \quad (8)$$

325 This mask isolates the region where the contrail was initially detected and is applied uniformly to all simulations to ensure spatial consistency. For each simulation i , the difference relative to the deposition-adjusted control simulation (CNTL-DA, described in the next section), which contains no contrails, is computed over the masked region $((\cdot)^M)$ as

$$\Delta \bar{I}_i(t) = \langle \overline{I_i(x, y, t) - I_{\text{CNTLDA}}(x, y, t)} \rangle^M, \quad I \in \{\text{TICD}, \text{IWP}\}. \quad (9)$$

where IWP is the ice water path.

330 This approach allows for a consistent assessment of contrail evolution across different emission regimes. Even for short-lived contrails, this approach enables analysis of how the initially contrail-affected region evolves, whether it transitions into contrail cirrus or dissipates completely.

2.0.2 Simulation configurations

335 Two control simulations were performed: CNTL and CNTL-DA. The setups are identical except that CNTL assumes a constant deposition coefficient ($\alpha_D = 1$), whereas CNTL-DA applies a variable α_D . Both use a part of the CoAT configuration, diagnosing contrail-forming regions and properties — such as contrail depth, ice particle survival (IPS), CINC, CQI — at each timestep, as if an A321 or B747 were present throughout the domain. This methodology provides insights into potential contrail formation areas within the domain. The outcomes of these simulations are discussed in Sections 3.1.3 and ???. Second, we performed simulations where the model utilized actual flight data to extract specific aircraft locations and timings. Contrail characteristics were then simulated exclusively along the recorded flight paths, based on the aircraft properties detailed in Table 2. These findings are elaborated in Section 3.2.1. aircraft were uniformly distributed across the model domain. FlightRadar24 tracks are excluded, so no explicit contrail ice is added to the P3 microphysics or advected by GEM (CoAT excluding flights). Both simulations use an emission index of $1 \times 10^{15} \text{ kg}^{-1}$, representing the HS regime. Sections 3.1.1–3.1.2 compare the ice-supersaturated regions between CNTL-DA and CNTL, while Section 3.1.3 examines the sensitivity of contrail formation and related properties to α_D .

345 Subsequent sensitivity experiments employ the full CoAT configuration, which includes FlightRadar24 tracks (Table 2; Fig. 1a), to analyze contrail occurrence and persistence under varying soot-emission regimes for flights overpassing Toronto near 14:00 UTC (Sections 3.2.1–3.2.3). When contrails form, the resulting contrail ice is added to the P3 ice category and advected. All sensitivity simulations use the DA configuration. The complete set of simulations and their configurations is summarized in Table 3.

Table 3. Summary of GEM simulations showing the use of deposition adjustment (DA), inclusion of FlightRadar24 tracks (CoAT incl./excl. flights), and emission index (EI) category for each soot regime (Very-High-Soot (VHS), High-Soot (HS), Normal-Soot (NS), Low-Soot (LS)). A checkmark denotes applicable configurations.

Simulation	DA	CoAT excl. flights	CoAT incl. flights	Emission Index (EI, kg ⁻¹)			
				1.22×10^{15}	1.0×10^{15}	2.8×10^{14}	6.44×10^{13}
CNTL	~	✓	~	~	✓	~	~
CNTL-DA	✓	✓	~	~	✓	~	~
DA-VHS	✓	~	✓	✓	~	~	~
DA-HS	✓	~	✓	~	✓	~	~
DA-NS	✓	~	✓	~	~	✓	~
DA-LS	✓	~	✓	~	~	~	✓

3 Results

3.1 Depositional-growth-Deposition adjusted sensitivity simulations

3.1.1 RH_i distribution: Sounding vs GEM

The approach examines the relationship between ice particle growth rates and RH_i by analyzing soundings and comparing them to ~~simulations from the GEM model~~ the GEM simulations (CNTL and CNTL-DA). The simulations are designed to illustrate how variations in ice particle growth rates, ~~through the variation in α_D~~ , influence RH_i. By contrasting the sounding observations with GEM under different growth rate scenarios, we aim to elucidate the impact of ice particle depositional growth on atmospheric humidity profiles. To account for uncertainty in balloon drift, a ~~305 km × 305 km~~ area surrounding balloon location while ascending was used to compile the vertical profile for each station in ~~GEM's the model~~ output, which is then compared to the soundings.

Figure 2 presents the RH_i distribution for sounding observations compared to GEM at 1200 UTC on 25 Nov 2023, considering pressure levels between 100 hPa and 600 hPa and temperatures colder than -38 °C. ~~The simulations capture the general distribution well below an As the~~ RH_i of 100% when compared to the all-soundings distribution. However, as approaches 100%, ~~GEM the CNTL simulation~~ underestimates the probability of higher RH_i values, ~~particularly in the supersaturation range~~, where it fails to capture the frequency and intensity of ice supersaturation events. The ~~combined sounding probability density of the soundings peaks at an RH_i distribution peaks at 100~~ of 102% and decreases to 122% and then gradually decreases ~~, reaching % beyond which sparse observations, primarily from the White Lake (DTX) sounding, are present, extending up to a maximum RH_i of 145~~ 148%.

The CNTL simulation follows a trend commonly observed in atmospheric models, where the RH_i distribution peaks around ~~100~~ 102% before sharply declining due to rapid humidity quenching by ice growth schemes (Kärcher et al., 2023) or models using saturation adjustment schemes (Tompkins et al., 2007; Gierens et al., 2020). Unlike models employing a saturation

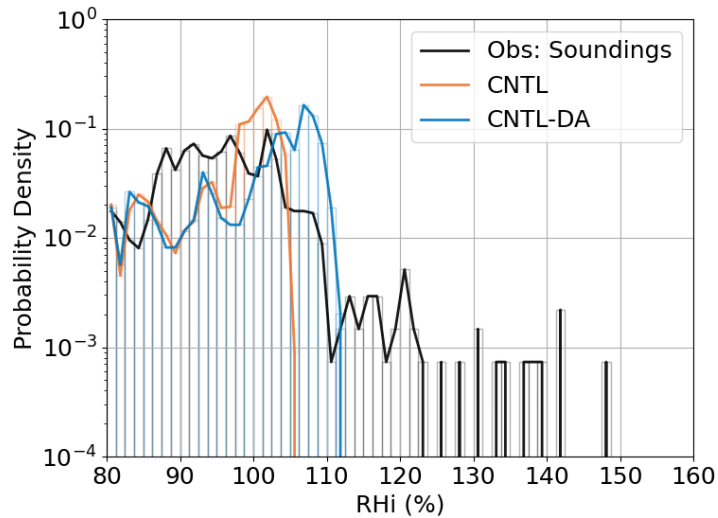


Figure 2. RH_i distribution for CNTL, ~~and~~ CNTL-DA simulations at 1200 UTC. The observations from all the radiosonde sounding is combined and shown as "Obs: Soundings" (black line). The GEM soundings include data in a 5 km × 5 km domain around the location of the balloon to account for uncertainty. All the data is limited for pressure levels between 100 hPa and 600 hPa and temperatures lower than -38 °C.

370 adjustment, ~~GEM's P3 microphysics scheme does not use~~ does not impose such a constraint. ~~When the depositional growth rate~~
~~is reduced to 90% () of the CNTL value, the~~ The CNTL-DA simulation exhibits a greater buildup of ice supersaturation due
~~to reduced depositional growth, producing a peak at RH_i distribution peak shifts from 100% to 104%, and the maximum~~
~~increases from 104% to ~ 108% .~~ Further reductions to 80 and a tail extending toward 113% () and 60% () enhance moisture
~~buildup, leading to higher maxima of 116% and 128%, respectively, which align more closely with observations. However,~~
375 ~~these reductions also lower the distinct 100% peak seen in the CNTL, suggesting a redistribution of humidity.~~ The largest
~~contributor to the underestimation is GEM's inability to capture the DTX sounding (Fig. B1).~~

3.1.2 The outlier: The White Lake (DTX) sounding

At the 500 hPa level, a deep trough was present over the Great Lakes region, indicating an area of lower pressure and cooler temperatures aloft (Fig. 1). This trough was associated with enhanced jet stream activity, which led to increased upper-level divergence. Such divergence promotes rising motion in the atmosphere, generating thin streaks of ice-supersaturated regions, which in turn favored cirrus cloud formation and the potential for persistent contrail development.

The DTX sounding profile reveals that the balloon drifted through one of these supersaturated streaks, recording RH_i values exceeding $\geq 140\%$ between 300–350 hPa and 200–250 hPa. While GEM—the CNTL-DA simulation accurately captured the broader upper-air trough, it failed to generate the highly ice-supersaturated regions above DTX (Fig. 3a). In contrast, most of the other stations, except for ALB, exhibited ice supersaturation. When the DTX station is excluded, CNTL-DA shows markedly improved agreement with observations (Fig. B1), capturing the ice-supersaturated layers between 400 hPa and 200 hPa observed at most other stations (i.e., Buffalo (BUF), which GEM represented better (e.g., Fig. 3b). However, this improved RH_i representation may be due to the fact that the because the other soundings did not contain such thick a large region with many thin layers of highly ice-supersaturated air, making them easier for the model to capture.

When the depositional growth rate is slowed the sensitivity simulations show a marginal improvement, with RH_i values increasing to 106% (–), 112% (–), and 122% (–). While this adjustment allows for a higher degree of ice supersaturation, the model still underestimates the extreme RH_i values observed in the DTX sounding, where RH_i exceeded 140% (Fig. 3a). In comparison, the ice-supersaturated regions are much better represented for the BUF sounding, especially in the – and – simulations. These slower deposition growth rates corresponds to α_d smaller than 0.1 for ice particle diameters of larger than 50 m (Fig. A1). There are very thin ice-supersaturated layers, such as at 220 hPa in Fig. 3b, which are not well represented in the GEM simulations. This discrepancy may be attributed to the vertical resolution of the model, where the layer thickness at this pressure level is approximately 250 m. The model's relatively coarse vertical resolution and unresolved subgrid-scale horizontal supersaturation inhomogeneity may smooth out small-scale supersaturation features, limiting its ability to resolve narrow layers of high RH_i . However, since RH_i in the CNTL-DA simulation remains well below the observed mean of 117% observed in the soundings% between 350 hPa and 250 hPa the discrepancy likely involves factors beyond vertical resolution.

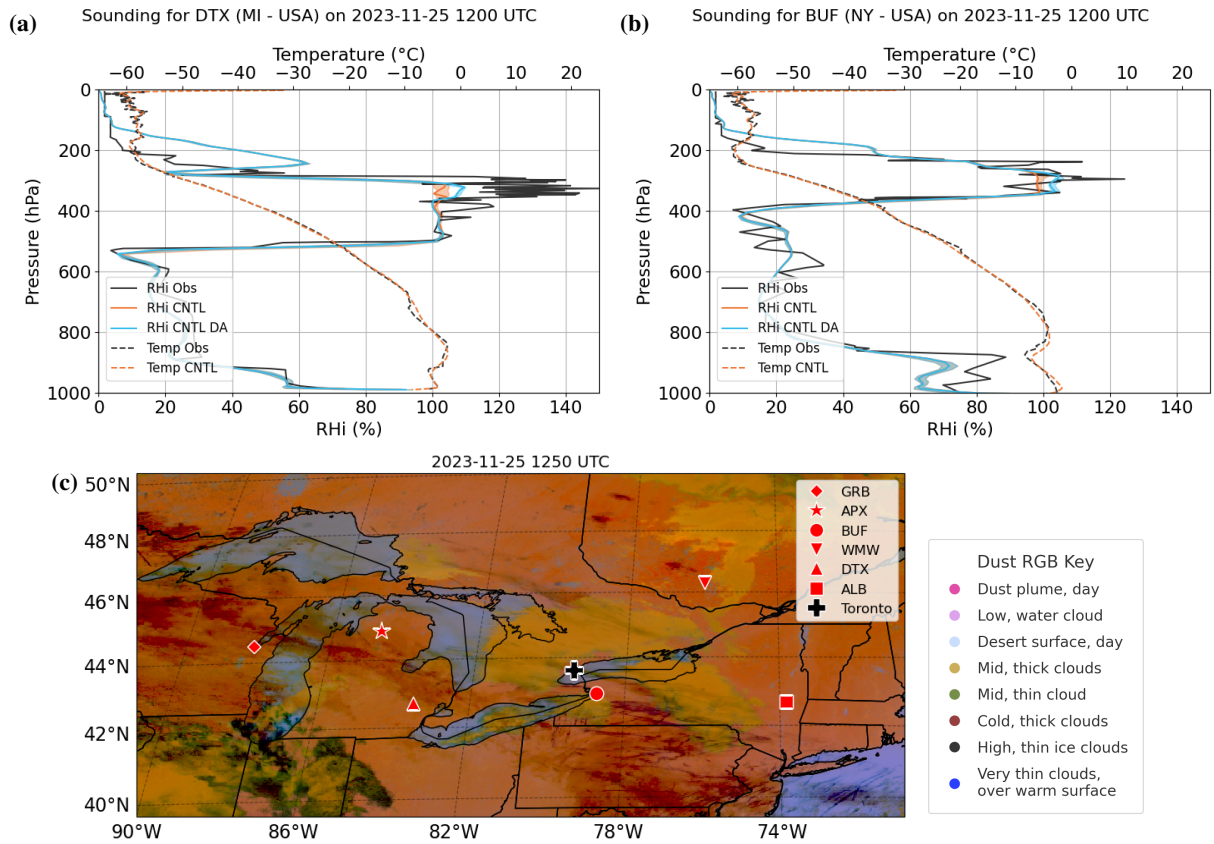


Figure 3. Soundings for (a) [White Lake \(DTX\)](#), (b) [Buffalo \(BUF\)](#) compared to the [-CNTL](#) and [-CNTL-DA](#) simulations. The shaded areas are the minimum and maximum values for a $5 \text{ km} \times 5 \text{ km}$ domain around the location of the balloon. Panel (c) is the GOES-16 Dust RGB at 1250 UTC. [The names of the abbreviated sounding stations \(red markers\) can be found in Table 1.](#)

3.1.3 GEM vs ceilometer observations at CYYZ

In the Great Lakes region, the interaction between cold Arctic air masses and the relatively warmer lake waters frequently triggers lake-effect snow events (Niziol et al., 1995). The synoptic conditions on 25 Nov 2023 and the following days facilitated such phenomena, leading to the formation of low clouds and heavy snowfall in the surrounding areas. On this day, these low clouds significantly attenuated the ceilometer signal ~~at CYYZ, Toronto,~~ making it nearly impossible to retrieve data from cirrus clouds between 1300 UTC and 1700 UTC ~~(Fig. 4)~~. However, a descending high cloud base was still noticeable, aligning with the descending moist layer observed in ~~all the CNTL and CNTL-DA simulations (Fig. 5)~~

~~a and b, top panels). The CNTL and CNTL-DA simulations show three panels each of time-height vertical profiles of RH_i and the corresponding CINC for A321 (middle panels) and B747 aircraft (bottom panels).~~ Between 1100 UTC and 1200 UTC, the ceilometer's backscatter intensity displayed a diffused structure, indicative of thin ice clouds like cirrus or contrails ~~around~~ ~ 10 km in altitude ~~(Fig. 4)~~. By 1200 UTC to 1300 UTC, the cirrus clouds became more structured, with a lower cloud base near 8 km, suggesting the presence of ice-supersaturated regions. ~~Figure 4 presents a time-series of the profiles for all simulations at the same location as the CYYX ceilometer.~~

The ~~and simulations support the presence of~~ ~~CNTL-DA simulation captures the~~ ice-supersaturated regions ~~between 8 and~~ ~~layer, favoring persistent contrail formation, between 8 km and 10 km, while the CNTL simulation shows no ice-supersaturation in this altitude range. Here, aircraft-specific differences become evident: the A321 forms contrails at $RH_i > 100$ km and indicate the potential for persistent contrail formation around ~ 100 km, whereas the heavier B747 requires $RH_i > 102$ km. In these marginally ice-supersaturated conditions, the B747's initial number of emitted ice crystals sublimates within the descending vortex. To produce contrails under the same ambient conditions (T, P, RH_i , atmospheric stability) observed between 1200 UTC and 1230 UTC, the B747 would require ambient temperatures ~ 2 °C lower.~~

From 1300 UTC until around ~~1500~~ ~~1445~~ UTC, ~~all simulations except failed to indicate~~ ~~neither of the simulations show~~ conditions suitable for persistent contrail formation. During this time, contrails were observed over Toronto (Fig. 1b to d), but images at 1420 UTC and simulations at 1400 UTC show no indication of new contrail formation, only widespread older contrails that had formed upstream towards the west.

~~Variations in the depositional growth rates of ice particles significantly affect the persistence and spatial extent of ice-supersaturated regions. While all sensitivity simulations indicate the presence of contrail-forming regions~~ ~~After 1445 UTC, the CNTL simulations exhibit conditions that are excessively dry prior to 1645 UTC. After this time, although simulation remains mostly ice-subsaturated to only weakly ice-supersaturated regions persists above 6 km, the ambient temperature remains too elevated, warmer than -45 (maximum $RH_i \approx 104$, for the aircraft plume to achieve supersaturation. Consequently, the nucleation and freezing of water droplets, essential for contrail persistence in ice-supersaturated environments, are inhibited. %), supporting only a shallow layer with a CINC of $\sim 0.4 \text{ cm}^{-3}$ for an A321 aircraft. In contrast, the reduced moisture deposition rate, synonymous to lower α_d values, in the sensitivity simulations allows for a more extensive and intense presence of~~ ~~CNTL-DA simulation develops a pronounced ice-supersaturated regions, thereby enhancing the likelihood of persistent contrail formation.~~

435 Time-series of ceilometer backscatter profiles for 25 Nov 2023 at Pearson International Airport (CYYZ, Toronto). The dotted lines indicate the descending cloud bottom and cloud top over time. The dashed line shows the altitude of the cloud bottom at 1200 UTC. The arrow indicates the low-level stratus between 1300 UTC and 1700 UTC.

Time-series for the for the (a) CNTL, (b) , (c) - and (d) -simulations between 1200 UTC and 1800 UTC. The grey shaded areas are the ice number concentration from ice clouds in the model. The dotted line one the where the temperature is -45 and the solid grey lines are the flight levels (FL).

440 3.2 CoAT simulations

3.1.1 Sounding vs CoAT

Here, we compare the atmospheric conditions at three sounding stations (ALB, BUF, and APX) spanning west to east along the main flight corridor at 1200 region (RH_i up to 112 UTC. The sounding data provide input for the CoAT model, which determines the formation of persistent contrail regions and evaluates contrail properties, such as contrail depth and CINC that survive the wake vortex. These simulations are then compared to results where the simulated atmospheric conditions from GEM serve as input for CoAT. For all comparisons, we assume the aircraft characteristics of an (%) conducive to persistent contrail formation near 10 km. Under these conditions, contrails from the A321 and only consider the simulation.

450 Figure ?? illustrates that flights traveling between ALB and BUF will begin to encounter high ice clouds. At ALB, the upper atmosphere remains dry and is not conducive to cirrus or contrail formation (Fig. ??a). In contrast, at BUF, between 400 hPa and 200 hPa, the observed appear first at RH_i exhibits significant variability, with multiple layers exceeding $\geq 100\%$, indicating the presence of ice-supersaturated regions. This is particularly pronounced between 300 hPa and 260 hPa, as well as in a very shallow layer at 240 hPa, where followed by those from the B747 around 1515 UTC as RH_i frequently surpasses 100 rises to $\approx 102\%$. In these regions, the ambient temperature is below the critical threshold for SAC, creating favorable conditions for persistent contrail formation (Fig. ??b).

455 While GEM generally captures the ice-supersaturated regions well, it does not fully resolve the magnitude of the observed supersaturation events, often smoothing out peaks where exceeds 100%. This discrepancy suggests that accurately capturing thin ice-supersaturated layers requires higher vertical resolution in models. The presence of highly localized supersaturation spikes (e.g. at 290 hPa) leads to CoAT generating deeper contrail depths and higher CINC of 310 m and 190 The CNTL-DA simulation produced deeper contrail forming region with enhanced CINC up to 1.4 cm^{-3} , respectively, compared to GEM-CoAT, which produced contrail depths and CINC of 160 m \in 100 m, 275 m and $60 \text{ cm}^{-3} \in 58 \text{ cm}^{-3}$, 80 cm^{-3} , respectively (BUF, Fig. ??b). for both aircraft types compared to the CNTL simulation.

465 It is important to note that in CoAT, SAC regions can be present even when the wake vortex model indicates no contrail formation (i.e., contrail depth and CINC of zero). This occurs because the wake vortex model accounts for adiabatic processes during plume descent, where warming of the air leads to ice particle sublimation. In this case, despite a temperature of -52 and an of 102.5% at a pressure of 270 hPa, all ice particles sublimated within the first few minutes of the young contrail's lifetime. This indicates that merely using SAC as an indicator for contrail persistence may overestimate the regions in which ice particles

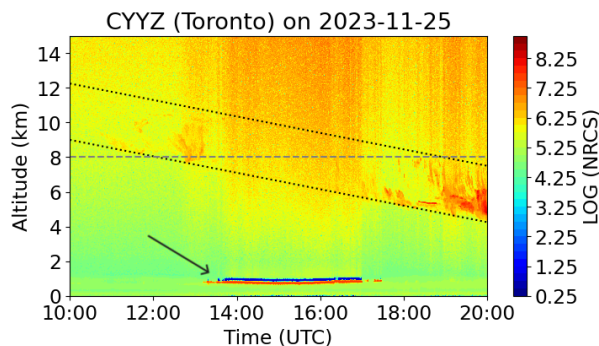


Figure 4. Time series of ceilometer's normalized range corrected signal (NRCS). The backscatter profiles are for 25 Nov 2023 at Pearson International Airport (CYYZ) in Toronto. The dotted lines indicate the descending cloud bottom and cloud top over time. The dashed line shows the altitude of the cloud bottom at 1200 UTC. The arrow indicates the low-level stratus between 1300 UTC and 1700 UTC.

can survive the wake-vortex dynamics. Overall, the CNTL-DA simulation captures deeper and more persistent contrail regions, consistent with its stronger and deeper ice-supersaturated layers.

470 In the case of the APX sounding (see Fig. ??c), the regions of supersaturation with respect to ice (SAC) appear to match reasonably well between the observational data and the GEM-CoAT simulation. However, the figure indicates that GEM-CoAT predicts a higher and more vertically extensive — from approximately 340 hPa to 240 hPa, compared to the narrower layer observed in the sounding data. As a result, GEM-CoAT overestimates both the contrail depth, generally simulating thicknesses between 250 m and 300 m, and the CINC. In contrast, CoAT typically shows contrail depths between 50 m and 100 m, except for one thin layer where the contrail depth reaches 225 m.

475 In general, an A321 aircraft operating along the ALB-BUF-APX corridor may have generated persistent contrails in the vicinity of the BUF and APX stations between 350 hPa and 250 hPa at 1200 UTC. Subsequently, at approximately 1300 UTC, flight DL384 traversed the Toronto region along the ALB-BUF-APX corridor at an altitude of \sim 300 hPa (30,000 ft). The analysis of this specific flight path is superimposed on the output of the model simulations, with the potential for contrail formation discussed in the following section.

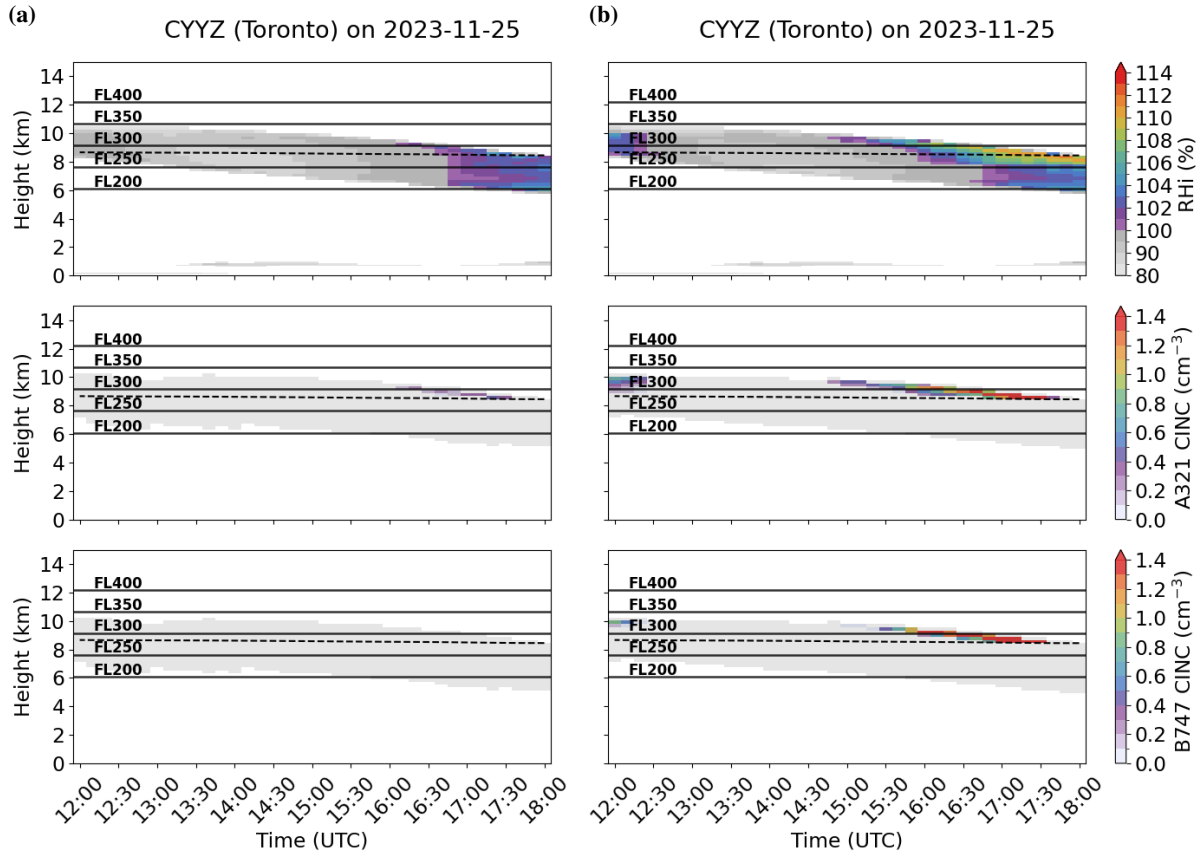


Figure 5. Time series for the RH_i for the (a) CNTL and (b) CNTL-DA simulations between 1200 UTC and 1800 UTC. The top panel shows the RH_i and the middle and bottom panels show the contrail ice number concentration (CINC) for an A321 and a B747 aircraft, respectively. The grey shaded areas are the ice number concentration from ice clouds in GEM. The dotted line one the where the temperature is -45°C and the solid grey lines are the flight levels (FL).

Atmospheric soundings for (a) ALB, (b) BUF and (c) APX compared to the GEM-CoAT simulation. The shaded areas are the minimum and maximum values for a $5\text{ km} \times 5\text{ km}$ domain around the location of the balloon. The shaded yellow and hatched areas are where persistent contrails can form according to the Schmidt-Appelman Criterion (SAC) in CoAT (calculated using the sounding information) and GEM-CoAT (calculated using the model data), respectively. The grey lines are the flight levels (FL).

3.2.1 Superimposed cross-section flight track analysis

In the following analysis, we compare the CINC produced along the A321 (medium-weighted category) flight path with those from a hypothetical B747 (heavy-weighted category) operating under identical meteorological conditions. This comparison isolates the influence of aircraft-specific wake dynamics and fuel flow rates on contrail ice production across different EI categories. Figure 6 illustrates the simulated cross-sectional regions of persistent contrail formation, highlighting areas where ice particles survive the wake vortex along the A321 flight route. (DL384) flight route (Figs. 1a and 6a). The aircraft, operating along the Albany-Buffalo-Gaylord (ALB-BUF-APX corridor, maintains) corridor, maintained an altitude of 300 hPa (30,000 ft) between -7474°W and -8484°W before ascending to 240 hPa (34,000 ft) at -8484°W , where it continues cruising. Over this cross-section, the CoAT simulation predicts young contrails with a CINC mean 10th percentile, 90th percentile of 83.9 cm^{-3} 62.8 cm^{-3} , 118.5 cm^{-3} (Figure 6a and b), then continued cruising.

During its cruise at 300 hPa, the A321 traverses traversed regions favorable for contrail formation, particularly over Lake Ontario as it approaches the approached the location of the APX station. Observations from GOES-16 Dust imagery confirm the presence of multiple aircraft-generated contrails between 1300 UTC and 1500 UTC (Figure 1). Near the location of the APX station, the A321 ascends out of the contrail-forming layer into a drier atmospheric region, where contrail formation ceases.

A comparison between the A321 (Figure 6b) and DA-HS simulation (B747 DA-HS) and the A321 CNTL (Figure 6d) reveals that the faster deposition growth CNTL simulation (B747 CNTL) exhibits a lower mean CINC (64.6 cm^{-3}). This trend is further supported by the significantly lower CINC 10th percentile in the A321 CNTL simulation (5.6 cm^{-3}), indicating a shallower distribution of ice particles under faster depositional growth rates. The reduction in ice particle survival is attributed to the enhanced moisture depletion in the ice-supersaturated regions due to faster deposition, leading to a decrease in, where the CNTL simulations use an EI = and ultimately lowering the ice number survival fraction during the wake vortex phase (Figure 6a and e). Consequently, $1 \times 10^{15}\text{ kg}^{-1}$, reveals pronounced differences in CINC and the extent of persistent contrail formation when the depositional mass growth of ice is adjusted by α_D (Figs. 6). The CINC is substantially reduced, and regions of persistent contrail formation are smaller, particularly in the B747 CNTL simulation. The contrast between two different aircraft in the CNTL simulation indicates that the B747 produces less persistent contrails than an A321 in similar meteorological conditions where $100\% \leq \text{RH}_i \leq 102\%$.

In the DA simulations, with enhanced RH_i , the regions of contrail formation become more consistent across aircraft and EI categories, and the main differences emerge in the CINC and IPS statistics. For example, in the DA-VHS simulation, the A321 CNTL simulation produces shallower contrails (detailed in the appendix) with lower contrail ice concentrations compared to the simulation, impacting the contrail's lifetime and evolution produces a mean CINC of 1.22 cm^{-3} with a mean IPS of 7.4 %, whereas the B747 yields a higher mean CINC of 1.90 cm^{-3} but a lower IPS of 6.41 % (Table 4).

When the With identical EIs, the mass fuel flow rate (m_f) differs markedly between aircraft — A321 aircraft (medium-weight category) is replaced by a: $m_f \approx 0.68\text{ kg s}^{-1}$ vs B747 (heavy-weight category) in the B747 and B747 CNTL simulations,

515 stark differences emerge: $m_f \approx 2.54 \text{ kg s}^{-1}$. The B747CNTL simulation indicates a significant reduction in the contrail
formation region, suggesting that heavy-weight category aircraft flying the same route and at the same time may form fewer
or no contrails compared to the medium-weight category aircraft (Figure 6d and h). The deeper wake generated by the's
stronger wake induces a deeper descent and adiabatic heating, enhancing sublimation and lowering IPS relative to the A321;
consequently, the contrail depth of the young contrail is shallower for the B747 results in increased adiabatic heating and
reduced ice particle survival, leading to a mean CINC of only 14.3 cm^{-3} compared to 64.6 cm^{-3} for the. Despite this, CINC
520 remains higher for the B747 because the higher mass fuel flow rate of the B747. That is, more particles are injected per meter of
flight, offsetting early losses and maintaining elevated CINC concentrations. This scaling also explains the observed cross-EI
relationships: in the DA-LS simulation, a B747 yields ICNC similar to an A321 (Table ??). A similar, though less pronounced,
reduction is observed between the in the DA-NS simulation, and similarly in the DA-NS simulation the CINC produced by a
B747 (61.1 cm^{-3}) and approaches the CINC produced by an A321C in the DA-HS simulation. Overall, a B747 using lean-burn
525 combustor producing lower soot ($\text{EI} = 6.44 \times 10^{13}$, DA-LS) can produce as many CINC as an A321 (83.9 cm^{-3}) simulations.

These findings highlight the role that aircraft weight, especially at near-ice-supersaturated conditions, and deposition growth
rates play in simulating contrail formation and persistence accurately. While faster deposition reduces contrail ice concentrations,
heavier aircraft further amplify this effect by increasing wake turbulence and adiabatic heating, ultimately limiting the conditions
necessary for persistent contrails operating with conventional JET-A fuel ($\text{EI} = 2.8 \times 10^{14}$, DA-NS).

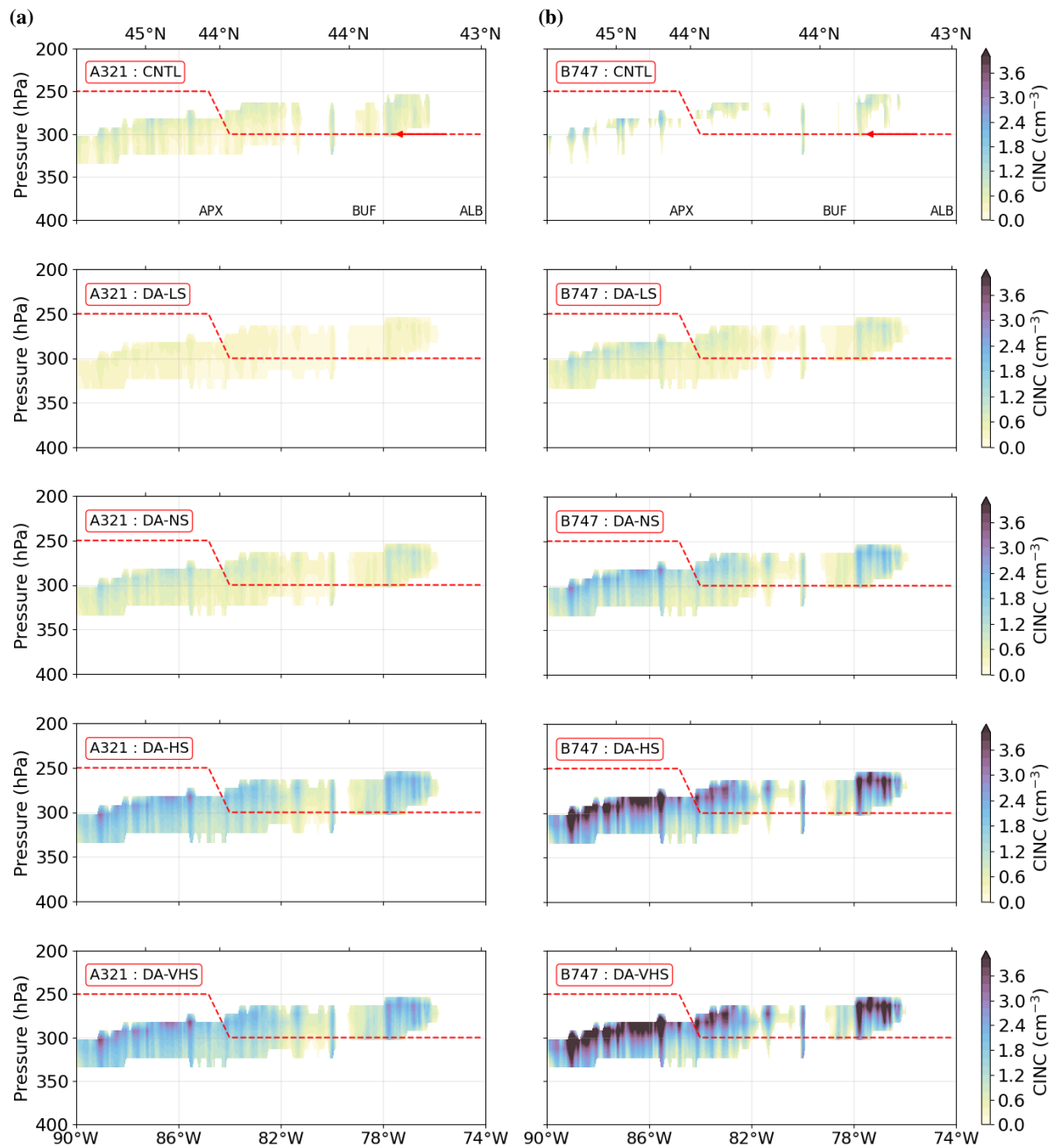


Figure 6. Vertical cross-section along the flight corridor (Albany–Buffalo–Gaylord; ALB–BUF–APX) indicated by the red dashes and red arrow for (a) an A321 and (b) a B747. The first panel in (a) and (b) is the CNTL simulation. The emission index categories (from the second to bottom panel) shown for (a) and (b) is Low-Soot (LS), Normal-Soot (NS), High-Soot (HS) and Very-High-Soot (VHS) using the deposition adjusted (DA) configuration. The flight paths are overlaid on regions depicting the contrail ice number concentration (CINC) at 1300 UTC.

Table 4. ~~Comparison of the A321 and B747 (in parentheses)~~ Contrail Ice Number Concentration (CINC) and ~~the~~ Ice Particle Survival (IPS) statistics (mean, 10th, and 90th percentiles) for ~~A321, A321-CNTL, B747, and B747-CNTL along young contrails (5 min) across emission indices (EI) for the flight route corridor in Figure Fig. 6. The EI categories are Very-High-Soot (VHS: $1.22 \times 10^{15} \text{ kg}^{-1}$), High-Soot (HS: $1.0 \times 10^{15} \text{ kg}^{-1}$), Normal-Soot (NS: $2.8 \times 10^{14} \text{ kg}^{-1}$), and Low-Soot (LS: $6.44 \times 10^{13} \text{ kg}^{-1}$).~~

Parameter	A321-0.8-DepDA-VHS	A321-CNTLDA-HS	B747-0.8-DepDA-NS	B747-CNTLDA-LS
CINC mean (cm^{-3})	83.9-1.22 (1.90)	64.6-1.06 (1.71)	61.1-0.46 (0.85)	14.3-0.18 (0.40)
CINC 10th perc (cm^{-3})	62.8-0.33 (0.40)	5.6-0.29 (0.39)	0.0-0.11 (0.22)	0.0-0.04 (0.12)
CINC 90th perc (cm^{-3})	118.4-2.10 (3.69)	87.8-1.84 (3.28)	88.3-0.82 (1.60)	65.8-0.35 (0.76)
IPS mean (%)	12.1-7.40 (3.30)	2.4-7.88 (3.63)	7.0-12.08 (6.41)	1.0-21.25 (13.21)
IPS 10th perc (%)	2.3-2.00 (0.69)	0.5-2.09 (0.82)	1.2-2.76 (1.64)	0.1-4.04 (3.81)
IPS 90th perc (%)	22.1-12.81 (6.41)	4.7-13.69 (6.99)	12.4-21.96 (12.17)	2.2-40.70 (25.11)

530 ~~Vertical cross-section along the flight path (ALB-BUF-APX) for (a) DL384 (A321), (b) DL384-CNTL (A321), (c) DL384 (B747) and (d) DL384 (B747) overlaid over regions showing the ice particle survival and contrail ice number concentration at 1300 UTC.~~

3.2.2 Contrail simulations in GEM-CoAT

In this section, we incorporate the flight information into GEM-CoAT using the aircraft characteristics listed in Table 2. We
535 simulate contrail formation based on the variation of aircraft properties and flight routes ~~from FlightRadar24.~~

From the GOES-16 observations and photographs (Fig. 1), it is evident that multiple aircraft-generated contrails were present over the Toronto area at 1420 UTC. Contrail formation began around 1200 UTC, increasing in extent and number until 1600 UTC. Here, we analyze the simulated contrails formed by ~~three-two~~ specific aircraft: TK6061 (B747), ~~-, flying northeastward) and DL384 (A321), and CV6686 (B747, flying westward). At 1420 UTC the contrail ages of the B747 and~~
540 ~~A321 are 35 min and 105 min, respectively (Fig. 7). The CINC produced by these aircraft is combined with the ice number concentration (INC) generated by GEM-P3's nucleation schemes generated by the ice nucleation parameterizations in P3 between 310 hPa and 290 hPa and where the $\text{RH}_i \geq 100\%$, to get the total ice number concentration (TINC), before being advected TICD. The simulated contrails are then compared with GOES-16 Dust observations at 1420 UTC.~~

Figure 7a highlights the ~~limitation of using standard depositional growth rates, as the CNTL simulation fails to reproduce~~
545 ~~any contrails over the domain at any time. Instead, it only represents INC from GEM-P3's ice nucleation scheme. In contrast, the simulation successfully contrasts between soot emission regimes across the different aircraft. The DA-LS simulation captures contrail formation, particularly from the TK6061 and DL384 aircraft, which were flying at for the B747 and A321 aircraft. The contrail generated by the B747, with $\text{TICD} \approx 240 \text{ cm}^{-2}$, is clearly distinguishable from the surrounding cirrus, whereas the contrail from the A321, with $\text{TICD} \approx 90 \text{ cm}^{-2}$, is only faintly visible within the cirrus at 1420 UTC. These flights~~
550 ~~operated at flight levels FL310 and FL300, respectively (Fig. 7b and Table 2). These aircraft overflew Toronto at 1345 UTC and 1245 UTC, respectively, while BUF soundings at 1200 UTC indicated persistent contrail formation regions between FL290~~

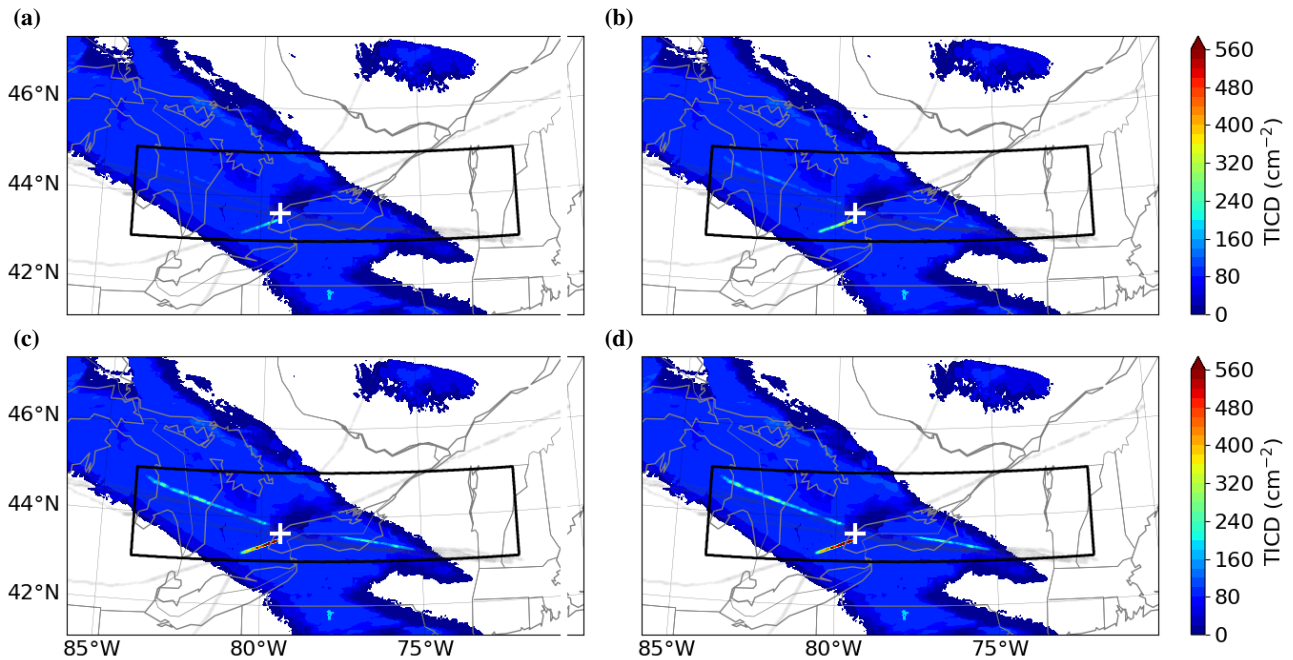


Figure 7. Combined Contrails from individual flights, where the contrail ice number concentration from GEM-P3 nucleation scheme and the GEM-CoAT scheme (CINC) is advected by GEM. The maximum total ice number concentration column density (TICD) is selected between 320 hPa obtained by adding the ice number concentrations from the GEM-P3 and 200 GEM-CoAT schemes within the 310 hPa and 290 hPa layer, where RH_i larger than 90% $\geq 100\%$, and the resulting TICD field is plotted. Flight information from Table 2 is used as input for the (a) CNTL and low-soot (DA-LS), (b) normal-soot (DA-NS), (c) high-soot (DA-HS), and (d) very-high-soot (DA-VHS) simulations at 1420 UTC. The flight tracks are shown in grey lines.

and FL330 (Fig. 3b). Additionally, CV6686 briefly formed a contrail north of Toronto, which dissipated within an hour due to its altitude at FL340, where it flew in and out of an ice-supersaturated layer. The locations of these As soot emissions increase, the TICD increases correspondingly, indicating greater persistence of the contrails (Figs. 7a to d). For example, for the A321, the TICD in the DA-VHS simulation is about 2.8 times higher compared to the DA-LS simulations, whereas the soot EI differs by nearly a factor of 19 for the same aircraft. Similarly, for the younger contrail from the B747, the TICD is about 3.2 times higher. This shows that although the soot EI directly influences the initial CINC, the resulting surviving ice crystals do not scale linearly with it (also true for a 5 min old contrail), because a significant fraction of particles are lost during the wake vortex descent. Consequently, the wake dynamics strongly modulate how much of the emitted soot ultimately forms surviving ice crystals. Therefore, in modeling approaches that prescribe contrail radiative properties based solely on the soot-derived ice number concentration, without accounting for wake-vortex losses, the simulated contrails may contain excessively small ice crystals, leading to biased radiative calculations.

In general, the locations of our simulated contrails from these aircraft align well with the contrails detected by GOES-16 Dust observations, a result that is only achieved when depositional growth rates are slowed in the DA simulations.

565 3.2.3 Contrail persistence under different soot regimes

570 The temporal evolution of contrail properties reveals clear differences in how soot emissions influence both the persistence of simulated contrails. Following the entry of flights DL384 and TK6061 into the model domain (black box in Fig. 7) at 1230 UTC and 1340 UTC, respectively, all sensitivity simulations show a rapid increase in TICD (Fig. 8b). Although the TICD is significantly larger than in the CNTL-DA simulation, the corresponding change in IWP remains insignificant compared to that of the pre-existing cirrus before 1400 UTC (Fig. 8a). Nevertheless, the enhanced TICD suggests that a greater number of contrail ice particles formed within the cirrus layer, which would amplify its radiative impact beyond that of the background cirrus. The magnitude and duration of these enhancements vary substantially across soot regimes. After 1400 UTC, both the IWP and TICD become significantly larger for the DA-VHS and DA-HS simulations compared to the CNTL-DA simulation. The DA-VHS simulation shows the strongest and most sustained increases in both TICD and IWP, reflecting high contrail ice crystal formation and slower dissipation. In contrast, the DA-LS simulation exhibits a much weaker response: its contrail dissipates progressively after 1400 UTC and becomes indistinguishable from the background variability of the CNTL-DA simulation by approximately 1645 UTC. This behavior highlights the sensitivity of contrail lifetime to soot availability, with reduced emissions leading to shorter-lived, less persistent contrails.

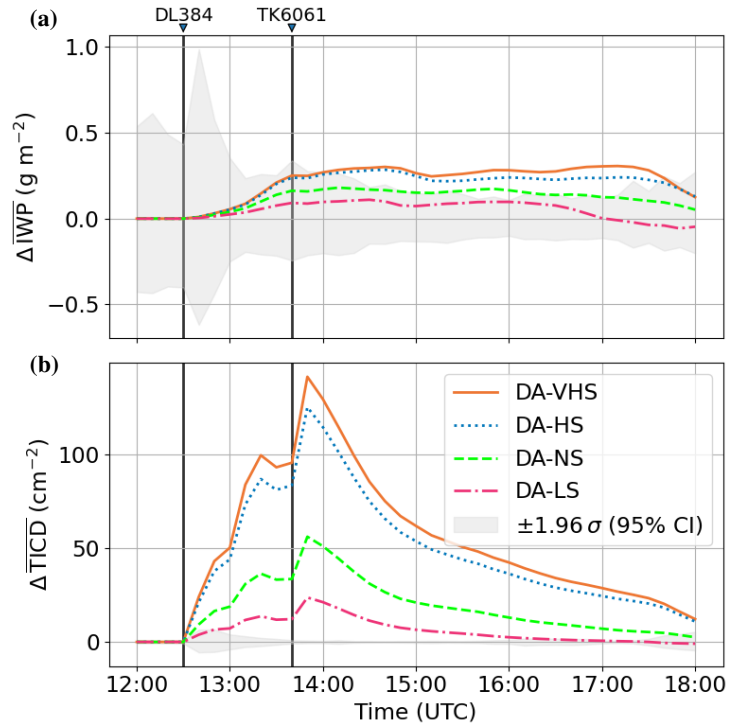


Figure 8. Contrail persistence showing the time evolution of mean differences of the (a) ice water path (IWP) and (b) total ice column depth (TICD) between the CNTL-DA and the sensitivity simulations (DA-VHS, DA-HS, DA-NS, DA-LS). The analyzed region is defined by grid points exceeding the 99.5th percentile of the DA-VHS simulation, which exhibited the longest-lived contrail. This mask is applied to all simulations to track the evolution of the contrail-affected region. Vertical lines indicate the passage times of flights DL384 and TK6061.

4 Summary and conclusions

580 On 25 November 2023, between 1200 UTC and 1800 UTC, widespread ice-supersaturated regions formed, resulting in a high occurrence of contrail formation over eastern Canada and the USA. Photographic images from Toronto and satellite-based observations from the GOES-16 Advanced Baseline Imager Dust Red-Green-Blue composite indicated that aviation contrails persisted for several hours, especially over the Lake Ontario region. Ceilometer data taken from Toronto Pearson International Airport (CYYZ), radiosonde soundings from Albany, Gaylord, Buffalo, White Lake, Green Bay, International Falls, Maniwaki, 585 and Pickle Lake were used to analyze the atmospheric conditions under which the ice-supersaturated regions formed.

The Global Environmental Multiscale (GEM) ~~model, which includes atmospheric model with~~ the Predicted Particle Properties (P3) microphysics scheme was employed as the base model ~~for to conduct~~ high-resolution simulations ~~of the event~~. The Contrail Avoidance Tool (CoAT) ~~, which consists of Schmidt-Appleman Criteria (SAC) and first applies the Schmidt-Appleman criterion (SAC Schumann, 1996) to identify regions favorable for contrail formation and then utilizes~~ the wake vortex model 590 ~~from, was used to determine persistent contrail forming regions and contrail properties (Unterstrasser, 2016) where both SAC and ice supersaturated conditions are met to diagnose persistent contrails and their properties under different soot emission regimes.~~

First, we analyzed the ability of GEM-P3 to simulate ice-supersaturated regions by ~~heuristically adjusting the including~~ ~~the deposition coefficient that slows the~~ depositional growth rate of ice particles ~~and to compare (deposition-adjusted control~~ 595 ~~simulation (CNTL-DA)) and compared~~ it against the ~~CNTL simulation, where no reduction factor was applied~~ control simulation (CNTL), ~~where the default deposition coefficient is unity~~. The findings can be summarized as follows:

- The CNTL simulation underestimates RH_i distribution, following a common trend in atmospheric models in which the moisture is quenched too quickly, resulting in a RH_i peak of ~~~100~~ ~102 %.
- ~~Sensitivity simulations indicate that reductions~~ ~~The CNTL-DA simulation indicates that reduction~~ in ice particle depositional growth ~~rates enhances rate enhance~~ moisture buildup, leading to improved forecasts of ~~the distribution peak at~~ RH_i ~108 % influencing the extent of contrail forming regions.
- ~~In CoAT, the presence of persistent contrail forming regions~~ ~~At Pearson International Airport, the CNTL simulation produced persistent contrail-forming regions only for the A321 (medium-weighted aircraft) and not the B747 (SAC) does not necessarily imply contrail formation, as wake vortex dynamics can induce adiabatic warming during plume descent, leading to complete ice particle sublimation despite favorable thermodynamic conditions. This suggests that SAC alone may overestimate the spatial extent of persistent contrail regions~~ ~~heavy-weighted aircraft), within a slightly ice-supersaturated layer ($RH_i \lesssim 102$ %) even where the SAC was satisfied. In contrast, the CNTL-DA simulation reached $RH_i \approx 112$ %, supporting persistent contrail formation for both the A321 and B747, although the B747 region was smaller.~~ 605

610 Second, the CoAT model was employed to simulate regions of persistent contrail formation and associated microphysical properties ~~for two aircraft types: the~~ ~~along the actual~~ A321 (medium-weight) and the B747 (heavy-weight), ~~along the~~

~~ALB-BUF-APX flight corridor~~ flight track obtained from FlightRadar24 on the Albany-Buffalo-Gaylord (ALB-BUF-APX) corridor, under multiple hypothetical soot emission regimes. A corresponding hypothetical B747 flight was simulated along the same track and soot regimes for comparison. The key ~~findings are~~ finding is summarized as follows:

- 615 – ~~In the simulations, the~~ At higher RH_i in the DA simulations, differences in contrail persistence diminish. The B747 ~~induces deeper wake vortices, leading to enhanced adiabatic heating and~~ maintains a higher contrail ice number concentration (CINC) because its higher fuel flow rate injects more soot particles per flight distance, offset by sublimation losses in the wake vortex. Consequently, a ~~subsequent 27% reduction in mean contrail ice number concentrations relative to the~~ low-soot B747 ($EI = 6.4 \times 10^{13} \text{ kg}^{-1}$) can produce CINC comparable to an A321 burning conventional Jet A fuel
620 ($EI = 2.8 \times 10^{14} \text{ kg}^{-1}$).

Lastly, we analyze the A321 and B747 flights overpassing Toronto, reproducing the contrail structure observed by GOES-16. These flights were simulated with CoAT under different soot emission regimes to assess the evolution of contrails from an older A321 contrail and a younger B747 contrail, providing insight into how soot regimes influence contrail development and persistence.

- 625 – Both flights show that total ice column density (TICD) increases with soot emissions but not linearly, due to wake-vortex-induced ice losses that limit the number of surviving ice crystals.
- ~~In the CNTL simulations, this reduction is even more pronounced at 78%, suggesting that heavier aircraft may significantly inhibit contrail formation under similar atmospheric conditions due to increased wake turbulence and ice particle sublimation.~~ Aircraft-specific wake dynamics and soot regimes jointly control ice crystal survival, indicating that contrail models
630 relying solely on a constant soot emission index as a proxy for contrail ice crystals, without accounting for wake-vortex losses, may overestimate small ice crystals and contrail radiative impacts.
- Among the sensitivity simulations, the very-high-soot regime produces the densest and most persistent contrails, sustaining significantly elevated TICD and ice water path (IWP) well beyond aircraft passage.
- Conversely, the low-soot regime generates fewer ice crystals and a weaker contrail that becomes indistinguishable from
635 the cirrus cloud at 1645 UTC.
- These contrasting behaviors indicate that higher soot emissions enhance contrail persistence and possibly radiative influence, while lower soot levels lead to shorter-lived, optically thinner contrails.

~~These results underscore~~ These results show the critical influence of aircraft-specific characteristics on contrail formation and persistence. More importantly, they demonstrate that ~~with a reduced~~ including ice crystal kinetics, represented by the
640 deposition coefficient, which reduced the depositional growth rate of ice particles, aided the GEM-CoAT model ~~was able to reproduce in reproducing~~ the observed contrails. This highlights the need to accurately represent ice supersaturation processes in numerical simulations to improve the fidelity of contrail modeling.

In this context, recent work on the introduction of the 3-moment treatment of ice in P3 by Milbrandt et al. (2021) has advanced the representation of microphysical processes, with P3 now fully 3-moment for all ice-related processes (Morrison et al., 2025). This allows the shape parameter of the ice size distribution, which is proportional to the relative spectral dispersion, to evolve independently for all processes, including depositional growth. As a result, the deposition rate both influences and is influenced by the shape parameter. Incorporating these interactions should, in principle, lead to a further improved representation of ice-supersaturated regions in the upper troposphere within GEM-P3. The underestimation of ice supersaturation in NWP models can be attributed to limitations in their representation of phase relaxation, turbulence, and layer resolution. Korolev and Mazin (2003) shows the important role of phase relaxation in regulating supersaturation within ice clouds. In typical cirrus conditions, where the ice crystal number concentration and size are approximately 200.2 cm^{-3} and 0.220 μm , respectively (Lohmann et al., 2016), the phase relaxation timescale is around 200 s. These timescales ~~can range between 60~~ are longer than the timesteps used in many NWP models (i.e. 30 s and 460 s in cirrus clouds, exceeding the timesteps commonly used in models. The substantially longer phase relaxation timescales allow supersaturation to persist beyond what is typically represented in numerical models. s in this study), meaning supersaturation could in principle be resolved explicitly. However, because most operational bulk microphysics schemes employ a saturation adjustment they tend to underestimate the buildup and persistence of ice supersaturation. Our CNTL simulation in GEM-P3 is unable to reproduce the buildup of supersaturation while using a 30 s model timestep, unless the ice deposition growth rate is adjusted. A limitation in the P3 ~~microphysics~~ scheme used in this study is its treatment of ice nucleation. While the scheme has undergone several improvements, the deposition nucleation process forms ice even at temperatures ~~colder~~ lower than -38°C , for which it was not originally designed. Additionally, the ice nucleation rate is currently set to $0.1 \text{ cm}^{-3}\text{s}^{-1}$, resulting in ice relaxation timescales of approximately 340 s, toward the lower end of the range associated with cirrus clouds. This may contribute to the model's inability to sustain elevated supersaturation levels. Ongoing work aims to refine the representation of ice nucleation at temperatures below -38°C , following approaches similar to those of Gasparini et al. (2025).

Another factor influencing the underestimation of ice supersaturation is the vertical grid spacing. Many global and regional climate models employ relatively coarse vertical layers, which ~~limit~~ limits their ability to resolve fine-scale turbulence and small-scale vertical motions that sustain localized supersaturation events. In coarse-resolution models, turbulence-induced variations in humidity tend to be smoothed out, leading to an ~~under-representation~~ underrepresentation of extreme supersaturation values (Burkhardt and Kärcher, 2009). This limitation becomes more pronounced when the Richardson number exceeds 0.25, which represents the ratio of buoyant energy to shear kinetic energy and determines the dynamic stability of the atmosphere (Stull, 2016). In such cases, significant wind shear within well-stratified layers can reduce the persistence of supersaturated regions (Thompson et al., 2024). Although GEM-P3 employs a relatively dense (compared to operational models) vertical grid spacing of 230 m in the upper atmosphere, our CNTL simulations still cannot reproduce the very shallow layers of elevated RH_i . This suggests that even relatively high-resolution models may struggle to capture the fine-scale structure of supersaturation layers, potentially contributing to the underestimation bias.

Code and data availability. Code will be made available after acceptance but can be showed to reviewers if desired. All data including those used to initialize the simulations, the simulated outputs, used in this study are archived internally for 5-year at the Canadian Meteorological Centre. The plotting software, GEM settings files and CoAT source code can be found at <https://doi.org/10.5281/zenodo.17820613>. The ceilometer and sounding data (University of Wyoming web site, <http://weather.uwyo.edu/>) can be found at <https://doi.org/10.5281/zenodo.15643030>.

Appendix A

A1 Depositional growth of ice particles

$$\frac{dm}{dt} = \frac{4\pi C(S_{v,i} - 1)}{\frac{\rho_i RT}{e_{\text{sat},i} D'_v M_w} + \frac{L_s \rho_i}{k'_a T} \left(\frac{L_s M_w}{RT} - 1 \right)}, \quad (\text{A1})$$

685 The equation describes the rate of mass growth of an ice particle, governed by the balance of vapor diffusion and heat conduction. The terms include the geometric capacitance C , supersaturation over ice $S_{v,i}$, ice density ρ_i , and saturation vapor pressure over ice $e_{\text{sat},i}$, along with the universal gas constant R , absolute temperature T , and water's molar mass M_w . The latent heat of sublimation L_s , thermal conductivity k'_a , and modified vapor diffusivity D'_v account for heat and mass transfer limitations in the crystal's growth process (Pruppacher and Klett, 2010).

$$690 \quad D'_v = \frac{D_v}{\frac{r}{r+\Delta_v} + \frac{D_v}{r\alpha_D} \sqrt{\frac{2\pi M_w}{RT_s}}}, \quad (\text{A2})$$

This correction to the standard diffusivity D_v incorporates only the kinetic effects and excludes ventilation, which is negligible for small ice crystals and thus disregarded (Pruppacher and Klett, 2010; Gierens et al., 2003). The key parameters in the kinetic correction factor include the crystal radius r and the "jump" distance Δ_v , typically set equal to the molecular mean free path. T_s represents the surface temperature of the growing ice crystal, and α_D is the deposition coefficient. α_D is defined via
695 the transcendental equation:

$$\alpha_{dD} = \left(\frac{s_{\text{sfc},d}}{s_{\text{crit}}} \right)^b \tanh \left[\left(\frac{s_{\text{crit}}}{s_{\text{sfc},d}} \right)^b \right] \quad (\text{A3})$$

which determines how efficiently water vapor deposits onto ice crystals. It depends on the local ice supersaturation at the crystal surface $s_{\text{sfc},d}$, the critical supersaturation s_{crit} , and a growth mechanism parameter b , which controls the transition between different crystal growth modes. The ice supersaturation $s_{\text{sfc},d}$ (Lamb and Verlinde, 2011) at the ice crystal surface and
700 the supercooling function s_{crit} based on the analysis of Zhang and Harrington (2014) and used by Kärcher et al. (2023)

$$s_{\text{sfc},d} = s \left(1 + \frac{\alpha_d r}{\ell} \frac{\alpha_D r}{\ell} \right)^{-1}, \quad s_{\text{crit}} / \% = 0.019655 \cdot (\Delta T / K)^{1.4305} \quad (\text{A4})$$

where s is the ambient supersaturation and ℓ the diffusion length. Similar to Kärcher et al. (2023) we define the transition growth regime with a size-dependent growth parameter m for spherical ice crystals:

$$b = \begin{cases} 1, & r < 10\mu m \\ 1 + 14 \left(\frac{r - 10\mu m}{70\mu m - 10\mu m} \right), & 10\mu m \leq r \leq 70\mu m \\ 15, & r > 70\mu m \end{cases} \quad (\text{A5})$$

705 In P3, the growth of ice particles follows the same formulation as in equation A1, but instead of using D'_v , the uncorrected diffusivity is used D_v , which is a function of temperature T and pressure P (Hall and Pruppacher, 1976). Consequently, we do not have an explicit description for α_D that can be directly modified to determine the depositional growth rate in P3.

To address this, ~~we solved equations A3, A4, and A5 were used to solve~~ for α_D ~~for across~~ ice crystal sizes between 1 and 200 μm using the ~~Newton-Raphson-Newton-Raphson~~ method, an iterative ~~numerical technique for finding the root of a~~
 710 ~~nonlinear equation and making an initial guess for root-finding technique initialized with $\alpha_D = 0.1$. The resulting $\alpha_D = 0.1$~~ (equations A3 and A4). The computed α_D values were then compared to a reference case ~~where with $\alpha_D = 1$, allowing us to evaluate the ratio between $(\frac{dm}{dt})_{\alpha_D}$ and $(\frac{dm}{dt})_{\alpha_D=1}$.~~

As shown in Figure A1, this ratio, referred to as the reduction factor for the depositional growth rate, ranges between 0.65 and 0.95 (Fig. A1). Therefore, we implemented reduction factors of 0.6 (\ominus), 0.8 (\ominus) and to compute the depositional mass growth ratio
 715 $(\frac{dm}{dt})_{\alpha_D} / (\frac{dm}{dt})_{\alpha_D=1}$, which depends on T , P , ice crystal size, and humidity. A 4-dimensional lookup table was constructed over the ranges $210 < T \text{ (K)} \leq 233$, $100 < P \text{ (hPa)} \leq 1000$, $100 < \text{RH}_i \text{ (%) } \leq 140$, and ice particle diameters from 1 to 200 μm . This lookup table was implemented in P3 to retrieve the depositional mass growth ratio and apply it as a multiplicative factor in the depositional mass growth equation. Figure A1 shows the results under typical cruising-altitude conditions. For example, in
 720 ~~in our sensitivity simulations and compared them to to 0.8, indicating a 10–20 % reduction relative to the reference case (CNTL) where $(\frac{dm}{dt})_{\alpha_D} = (\frac{dm}{dt})_{\alpha_D=1}$.~~ At $\text{RH}_i = 105 \%$ for the same particle sizes, the ratios decrease to 0.85–0.65, reflecting slower depositional growth.

A2 Contrail spread over multiple vertical levels

The fractional distributions, f_{r1} and f_{r2} , represent how the contrail ice is spread over multiple model levels. Specifically, f_{r1}
 725 is the fraction of contrail ice within the current model level, while f_{r2} accounts for the fraction extending beyond the current level into a lower model layer. These fractions are computed using the depth of the contrail ($\text{Cd}(k)$) and the depth of the model level ($\text{Zd}(k)$).

The total ice crystal number and ~~ice crystal~~ mass concentrations in a grid box are denoted by $N_{i_{\text{tot}}}(k)$ and $Q_{i_{\text{tot}}}(k)$, respectively. These quantities are updated by adding the contributions from contrail ice (~~$N_{i_{\text{contrail}}}(k)$ and $Q_{i_{\text{contrail}}}(k)$~~) CINC(k) and
 730 CQI(k) scaled by the fractional distribution f_{r1} . Similarly, the ice content and ice crystals in the level below the current one, represented by $N_{i_{\text{tot}}}(k-1)$ and $Q_{i_{\text{tot}}}(k-1)$, are updated based on the portion of contrail ice extending downward, governed by f_{r2} .

$$f_{r1} = \frac{\text{Zd}(k)}{\text{Cd}(k)}, \quad f_{r2} = \frac{\text{Cd}(k) - \text{Zd}(k)}{\text{Cd}(k)} \quad (\text{A6})$$

$$N_{i_{\text{tot}}}(k) = N_{i_{\text{tot}}}(k) + \underline{N_{i_{\text{contrail}}}} \cdot \underline{\text{CINC}(k)} \cdot f_{r1}, \quad Q_{i_{\text{tot}}}(k) = Q_{i_{\text{tot}}}(k) + \underline{Q_{i_{\text{contrail}}}} \cdot \underline{\text{CQI}(k)} \cdot f_{r1} \quad (\text{A7})$$

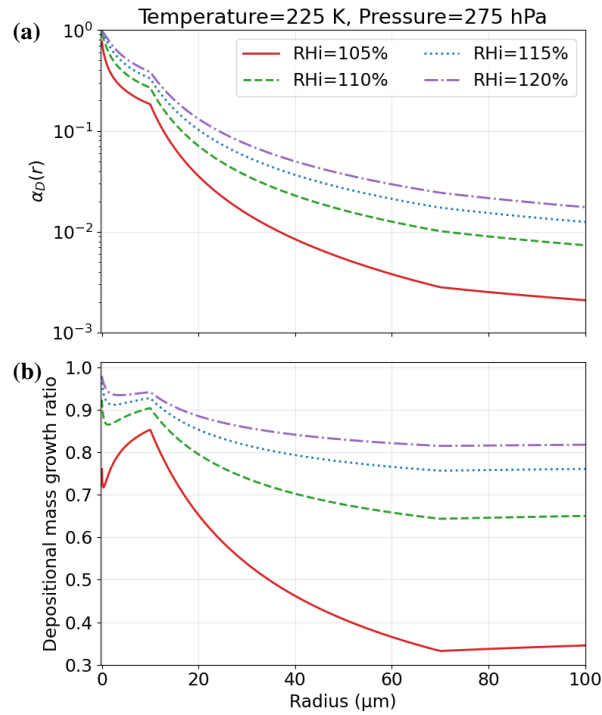


Figure A1. (a) The deposition growth coefficient (α_D) as a function of ice particle diameter, (b) relationship between α_D -radius and (c) the normalized deposition-depositional mass growth rate at $\alpha_D=1$, (d) deposition-rate-ratio defined as $(dm/dt)_{\alpha_D(r)}/(dm/dt)_{\alpha_D=1}$ as a function of α_D and (e) the ice particle diameter dependence on the normalized deposition-rate-ratio under varying atmospheric conditions.

$$735 \quad N_{i_{\text{tot}}}(k-1) = N_{i_{\text{tot}}}(k-1) + \underline{N_{i_{\text{contrail}}}} \underline{\text{CINC}}(k) \cdot f_{r2}, \quad Q_{i_{\text{tot}}}(k-1) = Q_{i_{\text{tot}}}(k-1) + \underline{Q_{i_{\text{contrail}}}} \underline{\text{CQI}}(k) \cdot f_{r2} \quad (\text{A8})$$

Appendix B

B1 Relative humidity distribution for radiosonde stations

740 Excluding the White Lake (DTX) station from the analysis yields a closer agreement between the CNTL and CNTL-DA simulations and the observational distribution. This discrepancy arises not from deficiencies in the sounding data, but from GEM's limited ability to represent the extreme ice-supersaturated conditions frequently observed over DTX.

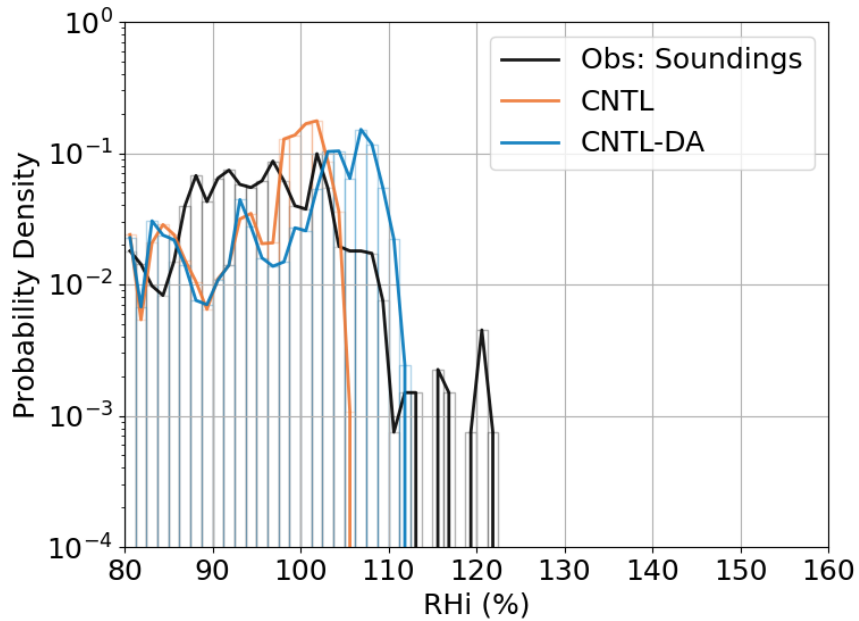


Figure B1. ~~Relative humidity with respect to ice~~ RHi distribution for CNTL, CNTL-DA simulations at 1200 UTC. The observations (excluding the White Lake (DTX) data) from all the radiosonde stations sounding is combined and shown as "Obs: Soundings" (black line). The ~~distributions only~~ GEM soundings include data ~~between pressures in a 5 km × 5 km domain around the location of 600~~ the balloon to account for uncertainty. All the data is limited for pressure levels between 100 hPa and ~~100~~600 hPa, and temperatures ~~colder~~ lower than -38°C .

Author contributions. ZD conducted the simulations and analyzed the results. ZD was the main author of the paper. AK, JM, ZD contributed to the study's design and the analysis of the results. All authors contributed to the study's writing.

Competing interests. The authors declare that they have no conflict of interest.

Acknowledgements. ZD acknowledge funding from Transport Canada under agreement STF22-010, and support from Environment and Climate Change Canada's Environmental Protection Branch. ZD also acknowledges and thanks FlightRadar24 for the usage of their proprietary data.

References

- Blaylock, B. K.: GOES-2-go: Download and display GOES-East and GOES-West data (Version 2022.07.15), <https://github.com/blaylockbk/goes2go>, 2023.
- 750 Burkhardt, U. and Kärcher, B.: Process-based simulation of contrail cirrus in a global climate model, *Journal of Geophysical Research: Atmospheres*, 114, <https://doi.org/10.1029/2008JD011491>, 2009.
- Burkhardt, U. and Kärcher, B.: Global radiative forcing from contrail cirrus, *Nature Climate Change*, 1, 54–58, <https://doi.org/10.1038/nclimate1068>, 2011.
- Burkhardt, U., Bock, L., and Bier, A.: Mitigating the contrail cirrus climate impact by reducing aircraft soot number emissions, *Climate and*
755 *Atmospheric Science*, 1, 1–7, <https://doi.org/10.1038/s41612-018-0046-4>, 2018.
- Cholette, M., Milbrandt, J. A., Morrison, H., Kirk, S., and Lalonde, L.-: Secondary Ice Production Improves Simulations of Freezing Rain, *Geophysical Research Letters*, 51, e2024GL108 490, <https://doi.org/10.1029/2024GL108490>, 2024.
- Côté, J., Gravel, S., Méthot, A., Patoine, A., Roch, M., and Staniforth, A.: The Operational CMC–MRB Global Environmental Multiscale (GEM) Model. Part I: Design Considerations and Formulation, *Monthly Weather Review*, 126, 1373–1395, [760](https://doi.org/10.1175/1520-)
[0493\(1998\)126<1373:TOCMGE>2.0.CO;2](https://doi.org/10.1175/1520-0493(1998)126<1373:TOCMGE>2.0.CO;2), 1998.
- Flightradar24: Live Flight Tracker - Real-Time Flight Tracker Map, <https://www.flightradar24.com/>, 2024.
- Fukuta, N. and Takahashi, T.: The Growth of Atmospheric Ice Crystals: A Summary of Findings in Vertical Supercooled Cloud Tunnel Studies, https://journals.ametsoc.org/view/journals/atms/56/12/1520-0469_1999_056_1963_tgoaic_2.0.co_2.xml, 1999.
- Gasparini, B., Atlas, R., Voigt, A., Krämer, M., and Blossey, P. N.: Tropical cirrus evolution in a km-scale model with improved ice micro-
765 physics, *EGUsphere*, pp. 1–34, <https://doi.org/10.5194/egusphere-2025-203>, 2025.
- Gierens, K., Matthes, S., and Rohs, S.: How Well Can Persistent Contrails Be Predicted?, *Aerospace*, 7, 169, <https://doi.org/10.3390/aerospace7120169>, 2020.
- Gierens, K. M., Monier, M., and Gayet, J.-F.: The deposition coefficient and its role for cirrus clouds, *Journal of Geophysical Research: Atmospheres*, 108, <https://doi.org/10.1029/2001JD001558>, 2003.
- 770 Girard, C., Plante, A., Desgagné, M., McTaggart-Cowan, R., Côté, J., Charron, M., Gravel, S., Lee, V., Patoine, A., Qaddouri, A., Roch, M., Spacek, L., Tanguay, M., Vaillancourt, P. A., and Zadra, A.: Staggered Vertical Discretization of the Canadian Environmental Multiscale (GEM) Model Using a Coordinate of the Log-Hydrostatic-Pressure Type, *Monthly Weather Review*, 142, 1183–1196, <https://doi.org/10.1175/MWR-D-13-00255.1>, 2014.
- Hall, W. D. and Pruppacher, H. R.: The Survival of Ice Particles Falling from Cirrus Clouds in Subsaturated Air, *Journal of the Atmospheric*
775 *Sciences*, 33, 1995–2006, [https://doi.org/10.1175/1520-0469\(1976\)033<1995:TZOIPF>2.0.CO;2](https://doi.org/10.1175/1520-0469(1976)033<1995:TZOIPF>2.0.CO;2), 1976.
- Harrington, J. Y. and Pokrifka, G. F.: An Approximate Criterion for Morphological Transformations in Small Vapor Grown Ice Crystals, <https://doi.org/10.1175/JAS-D-23-0131.1>, 2024.
- Jensen, E., Kaercher, B., Ueyama, R., and Pfister, L.: Ice Nucleation in the Tropical Tropopause Layer: Implications for Cirrus Occurrence, Cirrus Microphysical Properties, and Dehydration of Air Entering the Stratosphere, Chiba City, Japan, [https://ntrs.nasa.gov/search.jsp?R=](https://ntrs.nasa.gov/search.jsp?R=20170004663)
780 [20170004663](https://ntrs.nasa.gov/search.jsp?R=20170004663), 2017.
- Jensen, E. J., Kärcher, B., Woods, S., Krämer, M., and Ueyama, R.: The Impact of Gravity Waves on the Evolution of Tropical Anvil Cirrus Microphysical Properties, *Journal of Geophysical Research: Atmospheres*, 129, e2023JD039 887, <https://doi.org/10.1029/2023JD039887>, 2024.

- 785 Kalluri, S., Alcala, C., Carr, J., Griffith, P., Lebair, W., Lindsey, D., Race, R., Wu, X., and Zierk, S.: From Photons to Pixels: Processing Data from the Advanced Baseline Imager, *Remote Sensing*, 10, 177, <https://doi.org/10.3390/rs10020177>, 2018.
- Korolev, A., Qu, Z., Milbrandt, J., Heckman, I., Cholette, M., Wolde, M., Nguyen, C., McFarquhar, G. M., Lawson, P., and Fridlind, A. M.: High ice water content in tropical mesoscale convective systems (a conceptual model), *Atmospheric Chemistry and Physics*, 24, 11 849–11 881, <https://doi.org/10.5194/acp-24-11849-2024>, 2024.
- 790 Korolev, A. V. and Mazin, I. P.: Supersaturation of Water Vapor in Clouds, *Journal of the Atmospheric Sciences*, 60, 2957–2974, [https://doi.org/10.1175/1520-0469\(2003\)060<2957:SOWVIC>2.0.CO;2](https://doi.org/10.1175/1520-0469(2003)060<2957:SOWVIC>2.0.CO;2), 2003.
- Kärcher, B.: Formation and radiative forcing of contrail cirrus, *Nature Communications*, 9, 1824, <https://doi.org/10.1038/s41467-018-04068-0>, 2018.
- Kärcher, B. and Yu, F.: Role of aircraft soot emissions in contrail formation, *Geophysical Research Letters*, 36, <https://doi.org/08GL036649>, 2009.
- 795 Kärcher, B., Burkhardt, U., Bier, A., Bock, L., and Ford, I. J.: The microphysical pathway to contrail formation, *Journal of Geophysical Research: Atmospheres*, 120, 7893–7927, <https://doi.org/10.1002/2015JD023491>, 2015.
- Kärcher, B., Jensen, E. J., Pokrifka, G. F., and Harrington, J. Y.: Ice Supersaturation Variability in Cirrus Clouds: Role of Vertical Wind Speeds and Deposition Coefficients, *Journal of Geophysical Research: Atmospheres*, 128, e2023JD039 324, <https://doi.org/10.1029/2023JD039324>, 2023.
- 800 Lamb, D. and Verlinde, J.: *Physics and Chemistry of Clouds*, Cambridge University Press, Cambridge, <https://doi.org/10.1017/CBO9780511976377>, 2011.
- Lamb, K. D., Harrington, J. Y., Clouser, B. W., Moyer, E. J., Sarkozy, L., Ebert, V., Möhler, O., and Saathoff, H.: Re-evaluating cloud chamber constraints on depositional ice growth in cirrus clouds – Part I: Model description and sensitivity tests, *Atmospheric Chemistry and Physics*, 23, 6043–6064, <https://doi.org/10.5194/acp-23-6043-2023>, 2023.
- 805 Lee, D. S., Fahey, D. W., Forster, P. M., Newton, P. J., Wit, R. C. N., Lim, L. L., Owen, B., and Sausen, R.: Aviation and global climate change in the 21st century, *Atmospheric Environment*, 43, 3520–3537, <https://doi.org/10.1016/j.atmosenv.2009.04.024>, 2009.
- Lee, D. S., Fahey, D. W., Skowron, A., Allen, M. R., Burkhardt, U., Chen, Q., Doherty, S. J., Freeman, S., Forster, P. M., Fuglestvedt, J., Gettelman, A., De León, R. R., Lim, L. L., Lund, M. T., Millar, R. J., Owen, B., Penner, J. E., Pitari, G., Prather, M. J., Sausen, R., and Wilcox, L. J.: The contribution of global aviation to anthropogenic climate forcing for 2000 to 2018, *Atmospheric Environment*, 244, 810 117 834, <https://doi.org/10.1016/j.atmosenv.2020.117834>, 2021.
- Lee, D. S., Allen, M. R., Cumpsty, N., Owen, B., Shine, K. P., and Skowron, A.: Uncertainties in mitigating aviation non-CO₂ emissions for climate and air quality using hydrocarbon fuels, *Environmental Science: Atmospheres*, 3, 1693–1740, <https://doi.org/10.1039/D3EA00091E>, 2023.
- Lewellen, D. C.: Analytic Solutions for Evolving Size Distributions of Spherical Crystals or Droplets Undergoing Diffusional Growth in 815 Different Regimes, *Journal of the Atmospheric Sciences*, 69, 417–434, <https://doi.org/10.1175/JAS-D-11-029.1>, 2012.
- Lewellen, D. C.: Persistent Contrails and Contrail Cirrus. Part II: Full Lifetime Behavior, *Journal of the Atmospheric Sciences*, 71, 4420–4438, <https://doi.org/10.1175/JAS-D-13-0317.1>, 2014.
- Lewellen, D. C. and Lewellen, W. S.: The Effects of Aircraft Wake Dynamics on Contrail Development, *Journal of the Atmospheric Sciences*, 58, 390–406, [https://doi.org/10.1175/1520-0469\(2001\)058<0390:TEOAWD>2.0.CO;2](https://doi.org/10.1175/1520-0469(2001)058<0390:TEOAWD>2.0.CO;2), publisher: American Meteorological Society Sec- 820 tion: *Journal of the Atmospheric Sciences*, 2001.

- Lewellen, D. C., Meza, O., and Huebsch, W. W.: Persistent Contrails and Contrail Cirrus. Part I: Large-Eddy Simulations from Inception to Demise, *Journal of Atmospheric Sciences*, 71, 4399–4419, <https://doi.org/10.1175/JAS-D-13-0316.1>, 2014.
- Li, Y., Mahnke, C., Rohs, S., Bundke, U., Spelten, N., Dekoutsidis, G., Groß, S., Voigt, C., Schumann, U., Petzold, A., and Krämer, M.: Upper-tropospheric slightly ice-subsaturated regions: frequency of occurrence and statistical evidence for the appearance of contrail cirrus, *Atmospheric Chemistry and Physics*, 23, 2251–2271, <https://doi.org/10.5194/acp-23-2251-2023>, 2023.
- 825 Lohmann, U., Spichtinger, P., Jess, S., Peter, T., and Smit, H.: Cirrus cloud formation and ice supersaturated regions in a global climate model, *Environmental Research Letters*, 3, 045 022, <https://doi.org/10.1088/1748-9326/3/4/045022>, 2008.
- Lohmann, U., Lüönd, F., and Mahrt, F.: An introduction to clouds: From the Microscale to climate, Cambridge University Press, <https://doi.org/10.1017/CBO9781139087513>, 2016.
- 830 Lottemoser, A. and Unterstraßer, S.: High-resolution modelling of early contrail evolution from hydrogen-powered aircraft, *EGUsphere*, pp. 1–33, <https://doi.org/10.5194/egusphere-2024-3859>, publisher: Copernicus GmbH, 2025.
- Milbrandt, J. A. and Morrison, H.: Parameterization of Cloud Microphysics Based on the Prediction of Bulk Ice Particle Properties. Part III: Introduction of Multiple Free Categories, *Journal of Atmospheric Sciences*, 73, 975–995, <https://doi.org/10.1175/JAS-D-15-0204.1>, 2016.
- Milbrandt, J. A., Bélair, S., Faucher, M., Vallée, M., Carrera, M. L., and Glazer, A.: The Pan-Canadian High Resolution (2.5 km) Deterministic Prediction System, *Weather and Forecasting*, 31, 1791–1816, <https://doi.org/10.1175/WAF-D-16-0035.1>, 2016.
- 835 Milbrandt, J. A., Morrison, H., Ii, D. T. D., and Paukert, M.: A Triple-Moment Representation of Ice in the Predicted Particle Properties (P3) Microphysics Scheme, *Journal of the Atmospheric Sciences*, 78, 439–458, <https://doi.org/10.1175/JAS-D-20-0084.1>, 2021.
- Morrison, H. and Milbrandt, J. A.: Parameterization of Cloud Microphysics Based on the Prediction of Bulk Ice Particle Properties. Part I: Scheme Description and Idealized Tests, *Journal of the Atmospheric Sciences*, 72, 287–311, <https://doi.org/10.1175/JAS-D-14-0065.1>,
- 840 publisher: American Meteorological Society Section: *Journal of the Atmospheric Sciences*, 2015.
- Morrison, H., Milbrandt, J. A., and Cholette, M.: A Complete Three-Moment Representation of Ice in the Predicted Particle Properties (P3) Microphysics Scheme, *Journal of Advances in Modeling Earth Systems*, 17, e2024MS004644, <https://doi.org/10.1029/2024MS004644>, 2025.
- Niziol, T. A., Snyder, W. R., and Waldstreicher, J. S.: Winter Weather Forecasting throughout the Eastern United States. Part IV: Lake Effect Snow, https://journals.ametsoc.org/view/journals/wefo/10/1/1520-0434_1995_010_0061_wwfite_2_0_co_2.xml, 1995.
- 845 Pruppacher, H. R. and Klett, J. D.: *Microphysics of Clouds and Precipitation*, Atmospheric and Oceanographic Sciences Library, Springer Netherlands, 2 edn., 2010.
- Qu, Z., Korolev, A., Milbrandt, J. A., Heckman, I., Huang, Y., McFarquhar, G. M., Morrison, H., Wolde, M., and Nguyen, C.: The impacts of secondary ice production on microphysics and dynamics in tropical convection, *Atmospheric Chemistry and Physics*, 22, 12 287–12 310, <https://doi.org/10.5194/acp-22-12287-2022>, 2022.
- 850 Schumann, U.: On conditions for contrail formation from aircraft exhausts, *Meteorologische Zeitschrift*, pp. 4–23, <https://doi.org/10.1127/metz/5/1996/4>, publisher: Schweizerbart'sche Verlagsbuchhandlung, 1996.
- Schumann, U.: A contrail cirrus prediction model, *Geoscientific Model Development*, 5, 543–580, <https://doi.org/10.5194/gmd-5-543-2012>, 2012.
- 855 Seidel, D. J., Sun, B., Pettey, M., and Reale, A.: Global radiosonde balloon drift statistics, *Journal of Geophysical Research: Atmospheres*, 116, <https://doi.org/10.1029/2010JD014891>, 2011.

- Skrotzki, J., Connolly, P., Schnaiter, M., Saathoff, H., Möhler, O., Wagner, R., Niemand, M., Ebert, V., and Leisner, T.: The accommodation coefficient of water molecules on ice – cirrus cloud studies at the AIDA simulation chamber, *Atmospheric Chemistry and Physics*, 13, 4451–4466, <https://doi.org/10.5194/acp-13-4451-2013>, 2013.
- 860 Sperber, D. and Gierens, K.: Towards a more reliable forecast of ice supersaturation: concept of a one-moment ice-cloud scheme that avoids saturation adjustment, *Atmospheric Chemistry and Physics*, 23, 15 609–15 627, <https://doi.org/10.5194/acp-23-15609-2023>, 2023.
- Stull, R.: *Practical Meteorology: An Algebra-based Survey of Atmospheric Science*, AVP International, University of British Columbia, google-Books-ID: xP2sDAEACAAJ, 2016.
- Sussmann, R. and Gierens, K. M.: Lidar and numerical studies on the different evolution of vortex pair and secondary wake in young
865 contrails, *Journal of Geophysical Research Atmospheres*, 104, 2131–2142, <https://doi.org/10.1029/1998JD200034>, 1999.
- Teoh, R., Schumann, U., Majumdar, A., and Stettler, M. E. J.: Mitigating the Climate Forcing of Aircraft Contrails by Small-Scale Diversions and Technology Adoption, *Environmental Science & Technology*, 54, 2941–2950, <https://doi.org/10.1021/acs.est.9b05608>, 2020.
- Teoh, R., Schumann, U., Gryspeerdt, E., Shapiro, M., Molloy, J., Koudis, G., Voigt, C., and Stettler, M. E. J.: Aviation contrail climate effects in the North Atlantic from 2016 to 2021, *Atmospheric Chemistry and Physics*, 22, 10 919–10 935, <https://doi.org/10.5194/acp-22-10919-2022>, 2022.
870
- Thompson, G., Scholzen, C., O’Donoghue, S., Houghton, M., Jones, R. L., Durant, A., and Farrington, C.: On the fidelity of high-resolution numerical weather forecasts of contrail-favorable conditions, *Atmospheric Research*, 311, 107 663, <https://doi.org/10.1016/j.atmosres.2024.107663>, 2024.
- Tompkins, A. M., Gierens, K., and Rädel, G.: Ice supersaturation in the ECMWF integrated forecast system, *Quarterly Journal of the Royal
875 Meteorological Society*, 133, 53–63, <https://doi.org/10.1002/qj.14>, 2007.
- University of Utah: GOES-16/17/18 on Amazon Download Page, https://home.chpc.utah.edu/~u0553130/Brian_Blaylock/cgi-bin/goes16_download.cgi, 2020.
- University of Wyoming: Atmospheric Soundings, <https://weather.uwyo.edu/upperair/sounding.html>, 2024.
- Unterstrasser, S.: Large-eddy simulation study of contrail microphysics and geometry during the vortex phase and consequences on contrail-
880 to-cirrus transition, *Journal of Geophysical Research: Atmospheres*, 119, 7537–7555, <https://doi.org/10.1002/2013JD021418>, 2014.
- Unterstrasser, S.: Properties of young contrails; a parametrisation based on large-eddy simulations, *Atmospheric Chemistry and Physics*, 16, 2059–2082, <https://doi.org/10.5194/acp-16-2059-2016>, 2016.
- Unterstrasser, S. and Gierens, K.: Numerical simulations of contrail-to-cirrus transition – Part 1: An extensive parametric study, *Atmospheric
Chemistry and Physics*, 10, 2017–2036, <https://doi.org/10.5194/acp-10-2017-2010>, 2010.
- 885 Unterstrasser, S., Gierens, K., Sölch, I., and Lainer, M.: Numerical simulations of homogeneously nucleated natural cirrus and contrail-cirrus. Part 1: How different are they?, *Meteorologische Zeitschrift*, pp. 621–642, <https://doi.org/10.1127/metz/2016/0777>, 2017a.
- Unterstrasser, S., Gierens, K., Sölch, I., and Wirth, M.: Numerical simulations of homogeneously nucleated natural cirrus and contrail-cirrus. Part 2: Interaction on local scale, *Meteorologische Zeitschrift*, pp. 643–661, <https://doi.org/10.1127/metz/2016/0780>, publisher: Schweizerbart’sche Verlagsbuchhandlung, 2017b.
- 890 Zhang, C. and Harrington, J. Y.: Including Surface Kinetic Effects in Simple Models of Ice Vapor Diffusion, *Journal of Atmospheric Sciences*, 71, 372–390, <https://doi.org/10.1175/JAS-D-13-0103.1>, 2014.